NOVEL METHODS FOR ITERATIVE RECONSTRUCTION AND NOISE ESTIMATION IN CT IMAGING

A Dissertation
Presented to
The Academic Faculty

by

Tonghe Wang

In Partial Fulfillment
of the Requirements for the Degree
Doctor of Philosophy in the
School of Mechanical Engineering

Georgia Institute of Technology
August, 2017

NOVEL METHODS FOR ITERATIVE RECONSTRUCTION AND NOISE ESTIMATION IN CT IMAGING

Approved by:

Dr. Lei Zhu, Advisor
School of Mechanical Engineering
Georgia Institute of Technology

Dr. Justin Roper
School of Medicine
Emory University

Dr. C.-K. Chris Wang
School of Mechanical Engineering
Georgia Institute of Technology

Dr. John N. Aarsvold
School of Medicine
Emory University

Dr. Xiangyang Tang
Department of Biomedical Engineering
Georgia Institute of Technology

Date Approved: April 21, 2017

ACKNOWLEDGEMENTS

I express my special appreciation and thanks to my advisor Dr. Lei Zhu, who has been a tremendous mentor for me during my PhD study, for his patience and support on my work. I am very grateful to him for providing me invaluable advice and opportunities on both research and career.

I am also truly appreciate to my PhD reading committee, Dr. C.-K. Chris Wang, Dr. Justin Roper, Dr. Xiangyang Tang and Dr. John N. Aarsvold for their time and effort in reviewing this dissertation.

I thank my colleagues, Dr. Tianye Niu, Dr. Michael Petrongolo, Ms. Tiffany Tsui, Mr. Joe Harms and Dr. Linxi Shi for their encouragement and help in my work. Their useful advice and discussions have benefited me a lot.

I am especially grateful to my family and fiancee for their emotional and financial support throughout my PhD study. Their endless love and continued encouragement helps me persevere in my research. In addition, I thank my entire extended family for their support and love.

TABLE OF CONTENTS

LIST OF TABLES

LIST OF FIGURES

LIST OF SYMBOLS AND ABBREVIATIONS

ϵ	a small positive number to avoid singularities in the derivative calculation
λ	user-defined penalty weight on regularization term
ρ	mean electron density
$\boldsymbol{b}$	measured line integrals
$\boldsymbol{\mu}$	vectorized CT image
$\boldsymbol{\mu_H}$	vectorized image at high kVp
$\boldsymbol{\mu_L}$	vectorized image at low kVp
I	identity matrix
M	system matrix modeling CT forward projection
P	diagonal matrix
R	regularization term
W	similarity matrix
CS	compressed sensing
CT	computed tomography
DECT	dual-energy CT
FBP	filtered back-projection
GP-BB	gradient projection with an adaptive Barzilai–Borwein selection scheme
HU	Hounsfield unit
IR	iterative reconstruction
kV	kilovoltage
kVp	peak kilovoltage

MTF	modulation transfer function
NPS	noise power spectrum
OBI	on-board imager
PICCS	prior image constrained compressed sensing
PWLS	penalized weighted least-squares
RMSE	root mean square error
ROI	region of interest
SPIR	structure preserving iterative reconstruction
STD	standard deviation
TV	total variation
TVR	total variation regularization-based iterative reconstruction method

SUMMARY

Computed tomography (CT) has become an important clinical imaging modality, and has been extended into a wide range of usage with the development of novel CT scanners such as dual energy CT (DECT). However, the imaging dose during CT scanning increasingly raises public concern. Iterative reconstruction algorithms have shown promise on improving quality of CT images with reduced radiation. In the first part of this study, a novel iterative reconstruction method is developed to enable a new data acquisition scheme for potential reduction in imaging dose and engineering cost of DECT.

As iterative CT reconstruction continues to advance, the spatial distribution of noise standard deviation (STD) and accurate noise power spectrum (NPS) on the reconstructed CT images become important for method evaluation as well as optimization of algorithm parameters. In the second part of this study, a practical method for pixel-wise calculation of noise statistics on an iteratively reconstructed CT image is developed, which enables accurate calculation of noise STD for each pixel and NPS.

CHAPTER 1. INTRODUCTION

1.1 Computed tomography imaging

X-ray kilovoltage (kV) computed tomography (CT) imaging, first introduced by Godfrey Hounsfield into medical practice in 1971, has been widely studied and well developed for various clinical applications.[1] Its capability for producing detailed cross-sectional images of patients enables it to be one of the most popular clinical practices for diagnosis. In 2013, 43.5 CT scanners per million population are installed and 240 exams per 1000 population are performed in the United States, and the number of CT systems has been increasing by around 10% annually since the commercial introduction of multi-slice detector CT scanners.[2, 3] In addition to the regular diagnostic CT scanner, more advanced CT scanners are being introduced into extended special usage in radiology as well as radiation therapy, such as dual energy CT (DECT) for material decomposition and selective visualization or subtraction of iodinated contrast material.

1.1.1 Radiation dose concerns

The widespread use of CT raises the public concerns about the radiation dose deposited in patients during the scanning. The dose from CT examination accounts for more than two thirds of the total radiation dose from medical imaging.[4] Excessive CT dose leads to the increased risks of radiation-induced cancer and genetic defects.[5, 6] On the basis of risk estimates and data on CT use from 1991 through 1996, it has been estimated that about 0.4% of all cancers in the United States may be attributable to the radiation from CT studies. This estimate might have been in the range of 1.5 to 2.0% by 2007 due to the

increased use of CT.[7] Thus, methods to reduce the imaging dose as well as keep the image quality are very desirable in clinics.

Currently, CT dose can be lowered by optimizing data acquisition protocols (e.g. automatic exposure control),[8] improving detector designs and x-ray tube,[9-11] kV/spectrum shaping[12, 13], using reconstruction from reduced projection,[14] or applying noise suppression methods with degraded spatial resolution.[15] After continuous optimization of CT systems for decades, further dose reduction from these techniques is expected to be limited or costly. Efforts have been devoted to improvement of the method of image reconstruction from measured projection data with the increases in computing power.

1.1.2 Iterative reconstruction

Iterative reconstruction (IR) methods were proposed for image reconstruction in the early days of CT development in the 1970s.[1] However, its high computation and memory demands limited its practical usage in CT imaging in clinics. Instead, IR became a routine method for nuclear medicine emission tomography imaging modalities with lower spatial and temporal resolution, such as single photon emission CT and positron emission tomography, because of the smaller data volumes and less complex data handling.[16, 17] For CT imaging, the analytical method of filtered-back-projection (FBP) has become the standard reconstruction method due to its robustness and high speed in producing CT images in an adequate quality.

Despite its widespread usage, CT images reconstructed by FBP method can be affected by high image noise, artifacts (eg, streak artifacts), or poor low-contrast detectability in specific clinical scenarios.[16] It is because the FBP method is based on

simple mathematical assumptions that it may compromise the truthfulness of output images, such as infinitely small points of image pixels and perfect measurement without statistical fluctuations. The deviation in implementation of scanning from these ideal assumptions leads to high noise and severe artifacts on CT images. Such degraded image qualities become more severe when the CT imaging dose is reduced, which interferes with the delineation and low contrast detectability of structures. Although the imaging noise can be lowered by choosing a lower-frequency passing kernel in the FBP reconstruction process, the spatial resolution is impaired due to the characteristic of FBP that there is a trade-off between image noise and image sharpness.

These shortcomings in the FBP method have driven researchers to revisit IR for dose reduction in CT imaging. By modeling the physical process of a CT scan and incorporating prior knowledge, iterative CT reconstruction algorithms are found to be more resistant to noise and therefore require less imaging dose for the same image quality, compared with conventional analytical CT reconstruction. The IR method provides the flexibility to incorporate accurate models of each component of CT data acquisition such as scan geometry (i.e. finite size of focal spot), X-ray physics and detector response.[18] This part is usually called the data fidelity term. Moreover, a prior regularization on the distribution of the image space such as an image smoothness penalty can further control the image quality, which is called the regularization term. A commonly used prior model is a simple Markov random field with very local dependencies.[19, 20] Recent advances in the compressed sensing technique introduce the total variation (TV) regularization into IR, which assumes that the image boundary is sparse and enables high-quality CT reconstruction from noisy and highly undersampled projections.[21, 22] A typical IR method

is usually formulated as an optimization problem that minimizes the two part, i.e. the data fidelity term and the regularization term with the condition of image non-negativity. A weighting parameter is also applied on one of the terms to tune the image quality with different characteristics of images such as noise and spatial resolution.

On commercial CT scanners, a variety of vendor-specific IR methods have been implemented for clinical use. For example, GE Healthcare (Waukesha, WI) introduced their Adaptive Statistical Iterative Reconstruction (ASIR) in late 2008.[23] ASIR iteratively updates the image pixel values by comparing them with the ideal pixel values that are predicted with noise modeling until converge.[15] With the benefit of noise reduction, ASIR has been shown to reduce dose by up to 82% compared to standard FBP reconstruction at the same image quality.[24] Philips Healthcare (Best, the Netherlands) implemented iDose4 as IR in CT scanners in 2010. The iDose4 method analyzes, identifies and corrects the noisiest signal in measured projection data with a model of photon statistics. An iterative method is applied on the measured projection data to penalize those noisy data as well as preserve edges, followed by analytical image reconstruction. This method successfully prevents photon starvation artifacts,[25] and also achieves image noise reduction of 11% to 55% depending on the strength level of iDose4.[26] In 2010, Siemens Healthcare (Forchheim, Germany) released Sinogram-affirmed Iterative Reconstruction (SAFIRE), which utilizes both measured projection data and image data in two main loops. In the first loop, with an initial reconstruction using FBP method, SAFIRE first compares the forwarded projection from the FBP image with the original raw projection data to generate corrected projection for an updated FBP image. Such a loop is repeated several times. In the second loop, the noise is suppressed on the update FBP image from the first loop through a statistical

optimization process, which is also repeated several times.[27] It is found that the image noise can be reduced by 10% to 60% compared with FBP image depending on the iterative strength level.[16]

1.1.3 Noise estimation in iterative reconstruction

The knowledge of noise statistical properties of an algorithm is important for careful clinical evaluation as well as optimization of algorithm parameters. Despite the increasing number of publications on iterative CT reconstruction,[22, 28, 29] little research has been devoted to studies on noise statistical properties of these algorithms. A statistical analysis of CT image noise usually involves measurements of noise standard deviation (STD) and noise power spectrum (NPS). Noise STD quantifies the uncertainty level of pixel values, and is related to a wide range of image quality matrices such as signal-to-noise ratio. NPS describes the noise correlation among neighboring pixels and determines the noise texture of CT images.[30] As low-dose imaging protocols using iterative algorithms become more popular, a practical algorithm of noise STD map and NPS calculation on an iteratively reconstructed CT image could be a useful complementary tool in clinical practice. For example, an accurately measured noise STD map provides radiologists a reference map of reconstruction uncertainty during the diagnosis process. The NPS analysis aids radiologists to optimize the parameters of iterative reconstruction algorithms for a preferred noise texture. Moreover, the comparison of noise STD and NPS for different iterative reconstruction algorithms may help imagers choose the most suitable reconstruction method for a specific clinical task.

Accurate noise STD or NPS measurements require multiple scans on the same object without changing scan settings, which is considered impractical in clinical CT imaging. To estimate image noise statistics from a single CT scan, a commonly used method is to select a uniform region of interest (ROI) on the CT image, and then measure noise STD and NPS on the ROI, treating all the image pixels as random samples of the same probability distribution. This method inevitably lowers the spatial resolution of a STD map since a large size ROI is needed for accurate noise measurement. Furthermore, it is implicitly assumed that all image pixels of the ROI obey the same signal statistics. This assumption is inaccurate on a clinical image since the selected ROI does not always have uniform mean values and the noise level and spatial correlation vary across the entire image.

1.2 Dual energy CT

1.2.1 Principle

The concept of DECT was first proposed by R.E. Alvarez and A. Macovski in 1976.[31] In their original work, the principle of DECT is introduced: the attenuation coefficient of any material in the diagnostic energy range can be approximated as a weighted summation of two universal energy-dependent functions mainly accounting for photoelectric and Compton interactions. In practice, the basis functions can be the energy-dependent linear attenuation coefficients of two different actual or even virtual materials.[32] The weight distributions of the two basis functions, i.e., the decomposed material images, are reconstructed from the data acquired with two different x-ray energy spectra, which can be used to calculate electron density maps or effective Z images.[31]

The decomposition process can be implemented in either the projection domain or the image domain. The projection domain method, which is proposed from the original concept of DECT, requires acquisition of projection data with two different x-ray energies for each projection ray. Non-linear decomposition is then applied on the projection data to obtain the sinogram of two basis materials, from which decomposed materials are reconstructed via the same CT reconstruction principle. Since the decomposed images are energy-independent, these images are free from beam-hardening artifacts. However, for DECT scanners of some designs and scanning schemes, it is difficult or impossible to have dual-energy measurements on the same projection ray due to engineering issues. The procedure of material decomposition is therefore more conveniently performed on CT images after the standard CT reconstruction, typically based on a linear model,[33-36] at the price of losing the beam-hardening correction capability. Compared with the projection domain method, which usually requires the knowledge of x-ray spectra and detector response, or detailed calibration data with complex non-linear decomposition model, the image domain method is much easier to implement, thus is more commonly used on current commercial DECT scanners.[37]

In the existing literature,[34, 36] the terminology of DECT has extended from its original concept to include these imaging modalities based on image-domain decomposition.

1.2.2 Implementation of DECT on commercial CT scanners

Implementations of DECT highly depend on the specific designs of hardware and the scan schemes of the CT scanners. On a conventional diagnostic CT scanner, the

projection data at two different energy levels are measured by two sequential scans (so-called rotation-rotation mode) with two different kVps of X-ray tube, thus different energy spectrum. However, this method is very sensitive to patient motion because the time interval between the two kVps is in the order of seconds, which may cause motion-induced artifacts such as blurring of edges and steaks.[38] On the Aquilion ONE CT scanner of Toshiba America Medical Systems (Tustin, CA), this method is slightly improved by alternating the X-ray tube potential between high and low kVps with each gantry rotation instead of each scan. This is shown in Figure 1.1. However, it still has the worst temporal resolution compared with other commercial DECT scanners.

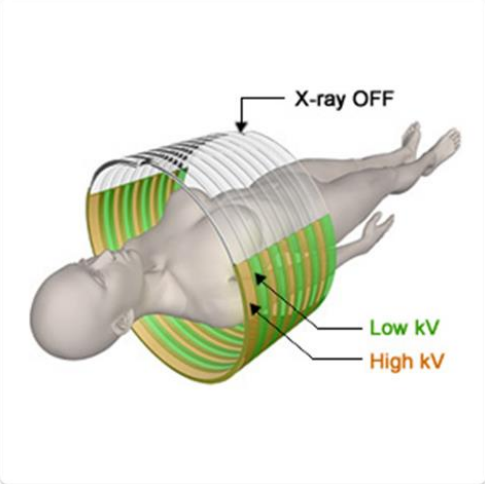

Figure 1.1 Implementation of DECT by two sequential scans of different kVps on Aquilion ONE CT scanner of Toshiba America Medical Systems. (http://www.toshiba-medical.eu/eu/product-solutions/computed-tomography/aquilion-one/aquilion-one-advanced-applications/)

On the HD 750 CT scanner from GE Healthcare, a fast-kVp switching method is successfully implemented. [39] As shown in Figure 1.2, it acquires dual-energy projections in one single rotation via rapidly switching the potential of X-ray tube between low- and high- kVps in adjacent views, which enables accurate spatial-temporal registration between

two different kVps, thus freezing motion and significantly reducing artifact. Since data acquisition is doubled without increasing scan time, the scanner is equipped with a fast detector and a fast-switching high-voltage generator, both of which significantly increase the system cost.

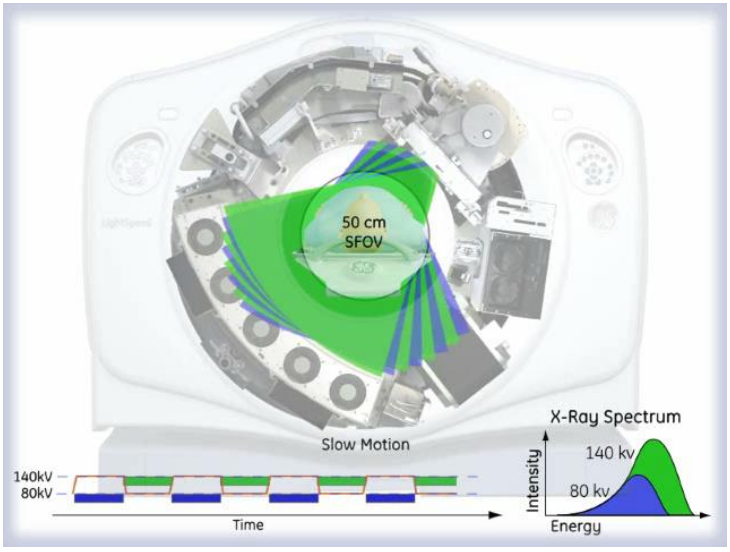

Figure 1.2 Implementation of DECT by fast-kVp switching method on HD 750 CT scanner from GE Healthcare. (http://www3.gehealthcare.com.au/en-au/products/categories/computed_tomography/discovery_ct750_hd/spectral_imaging)

For Siemens Healthcare, the design of dual sources is implemented on their several DECT scanners: Somatom Definition DS in 2006, Somatom Definition Flash in 2009 and Somatom Force in 2013.[40] On dual-source CT, two pairs of x-ray source and detector are mounted orthogonally on the same gantry as shown in Figure 1.3.[41] The advantage of dual-source CT is that both x-ray tube potential and the tube current can be independently controlled to optimize the spectral filtration for each tube-detector pair, which enables increased spectral separation and an increased signal-to-noise ratio in the material-specific images.[40, 42, 43] However, since the two x-ray tubes are in operation simultaneously, the

photon emitted from one tube may be detected by the detector of the other tube-detector pair, which degrades the spectral separation.[44]

Figure 1.3 Implementation of DECT by dual-source CT on Somatom Force CT scanner of Siemens Healthcare. (https://www.healthcare.siemens.com/computed-tomography/dual-source-ct/somatom-force/technical-specifications)

A dual-layer scintillation detector has been used on IQ on spectral CT system of Philips Healthcare for DECT. [45-47] With a single high tube potential, the dual-layer detector collects low-energy projections from front layer and the high-energy projections from the back layer. The advantage of this method is that the low- and high-energy projections are acquired simultaneously, which allows excellent temporal matching. However, the sensitivity profiles of the available materials on the detector layers have a rather broad overlap on X-ray energy spectrum, which limits the contrast of the spectral information or requires a relatively high additional dose.[48]

1.2.3 Clinical application

DECT has been increasingly used in different clinical applications. For example, bones and iodinated vessels usually have very similar ranges of Hounsfield Units (HU) on

CT images, which makes them difficult to be differentiated. By identifying and removing bones from iodinated vessels with material decomposition, DECT can resolve the superimposition of bone and vessels and generate direct angiography images. [49-52] DECT can also be used to assess lung perfusion with significantly reduced imaging dose compared to dynamic CT. [53, 54] In the abdomen area, DECT is able to identify the renal calculi and differentiate uric acid stone and non-uric acid stone. [55-57]

In DECT, the decomposed material images reconstructed from the data acquired with two different x-ray energy spectra, can be used to calculate electron density maps which is important in dose calculation for radiation therapy.[31, 58] Recent studies show DECT can be further used to estimate the proton stopping power ratio distribution inside a patient, which may play an important role in proton therapy treatment planning.[59]

Another common application of DECT is to generate virtual unenhanced CT images. DECT can identify and remove the iodine component from CT images to create images without contrast material enhancement. Thus, the true scan without contrast of multiphase examinations can be skipped if the virtual unenhanced image has satisfactory quality. It is very attractive in the CT evaluation of the kidneys, ureters, and bladder which include a complete examination with both a noncontrast and a contrast-enhanced scan.[40, 60-62]

1.3 Main contributions and publications

Most of the work in this dissertation can be found in the following journal papers and conference proceedings:

T. Wang and L. Zhu, "Dual energy CT with one full scan and a second sparse-view scan using structure preserving iterative reconstruction (SPIR)," Physics in Medicine and Biology 61, 6684 (2016)

T. Wang and L. Zhu, "Pixel-wise estimation of noise statistics on iterative CT reconstruction from a single scan", in press, Medical Physics, (2016)

J. Harms, **T. Wang**, M. Petrongolo, T. Niu, and L. Zhu "Noise suppression for dual-energy CT via penalized weighted least-square optimization with similarity-based regularization" Medical Physics, 43, 2676-2686 (2016)

J. Harms, **T. Wang**, M. Petrongolo, and L. Zhu "Noise suppression for energy-resolved CT using similarity-based non-local filtration" Proc. SPIE 9783, Medical Imaging 2016: Physics of Medical Imaging, 978341 (March 31, 2016)

as well as conference presentations:

T. Wang and L. Zhu "Pixel-wise calculation of noise statistics on iterative CT reconstruction from a single scan", talk in 58th AAPM Annual Meeting, July 2016, Washington, DC

T. Wang and L. Zhu "Dual energy CT with one full scan and a second sparse-view scan using structure preserving iterative reconstruction (SPIR)", talk in 57th AAPM Annual Meeting talk, July 2015, Anaheim, CA.

T. Wang and L. Zhu "Dual energy CT using one full scan and a second scan with very few projections", talk in 56th AAPM Annual Meeting, July 2014, Austin, TX.

1.4 Outline of this dissertation

The dissertation is organized in the following manner:

Chapter 1 gives an introduction of the background and scope of this dissertation, and outlines the dissertation

Chapter 2 introduces a novel iterative reconstruction method for DECT to enable a new data acquisition scheme which requires one full scan and a second sparse-view scan for potential reduction in imaging dose and engineering cost of DECT.

Chapter 3 presents a practical method for pixel-wise calculation of noise statistics on an iteratively reconstructed CT image, which enables accurate calculation of noise standard deviation for each pixel and noise power spectrum.

Chapter 4 summarizes the dissertation and suggests directions for future research.

CHAPTER 2. DUAL ENERGY CT WITH ONE FULL SCAN AND A SECOND SPARSE-VIEW SCAN USING STRUCTURE PRESERVING ITERATIVE RECONSTRUCTION (SPIR)

2.1 Introduction

Dual energy CT (DECT) has been increasingly used in different clinical applications, including direct angiography and bone removal,[49-52] assessment of lung perfusion,[53, 54] characterization of renal calculi,[55, 56] and generation of virtual unenhanced CT images.[60] Conventional DECT reconstruction theory requires two full-size projection datasets with two different energy spectra. This chapter aims to relax the data acquisition requirement of DECT for potential dose reduction and simplified imaging schemes by using an iterative reconstruction algorithm, which exploits the redundant structural information of the CT images acquired at two different x-ray energies.

The DECT theory assumes that the attenuation coefficient of any material in the diagnostic energy range can be approximated as a weighted summation of two universal energy-dependent functions mainly accounting for photoelectric and Compton interactions.[31] In practice, the basis functions can be the energy-dependent linear attenuation coefficients of two different actual or even virtual materials.[63] The weight distributions of the two basis functions, i.e., the decomposed material images, are reconstructed from the data acquired with two different x-ray energy spectra, which can be used to calculate electron density maps or effective Z images.[31] The original concept of DECT requires acquisition of projection data with two different x-ray energies for each

projection ray. Non-linear decomposition is then applied on the projection data to obtain the sinogram of two basis materials, from which decomposed materials are reconstructed via the same CT reconstruction principle. In practical implementations of DECT, dual-energy projection data can be acquired, for example, on advanced CT imaging systems, including dual-source CT[41] or fast kVp switching CT,[39, 64] or using two sequential scans (so-called rotation-rotation mode) on a conventional diagnostic CT scanner. In these data acquisition schemes (except using a dual-layer detector as on the Philips IQon spectral CT system[45-47]), however, it is difficult or impossible to have dual-energy measurements on the same projection ray. The procedure of material decomposition is therefore more conveniently performed on CT images after the standard CT reconstruction, typically based on a linear model,[33-36] at the price of losing the beam-hardening correction capability. In the existing literatures,[34, 36] the terminology of DECT has extended from its original concept to include these imaging modalities based on image-domain decomposition. This chapter follows the convention and refer to all imaging systems that acquire projection data with two effective x-ray spectra and perform material decomposition as DECT systems, although readers should be aware that DECT in the strict sense uses only non-linear decomposition in the projection domain.

DECT requires doubling the size of projection measurements. In current DECT implementations, this condition is satisfied by either scan time increase, as in the rotation-rotation mode on a conventional diagnostic CT scanner, or hardware advancements, as on the dual-source CT,[41] the fast kVp switching CT[39] and the dual-layer detector CT.[45, 46] This work focuses on a software-based improvement to reduce the requirement of data acquisition for DECT. A new reconstruction algorithm is developed using a full CT scan

plus a second scan with very few projections for high-quality DECT, which potentially reduces imaging dose and allows for more flexible designs of data acquisition on clinical DECT systems. This proof-of-concept investigations are performed on DECT using a rotation-rotation mode, i.e., two sequential CT scans at different x-ray energies, with image-domain decomposition. The proposed method is expandable to other DECT imaging modalities using either image-domain or projection-domain decomposition.

Iterative algorithms have demonstrated successes on CT reconstruction on sparse data.[21, 22, 65-72] The projection data for high-quality CT images are further reduced if the reconstruction is constrained by prior images, as shown in many recent applications, including 4D CBCT,[73] daily imaging CBCT,[74, 75] and cardiac CT.[76, 77] An iterative algorithm is developed to improve DECT on sparse data with a design strategy different from those of existing algorithms. In this new DECT reconstruction method, a full scan is first used to obtain an estimated classification of object structures. A bilateral filter is calculated as a similarity matrix from the first full-scan CT image to quantify the similarity between any two pixels. This similarity matrix remains approximately unchanged on the same object in different CT scans, although the CT image pixel values may vary. In a second CT scan with different x-ray energy and significantly reduced projections, a high-quality CT image is reconstructed by an iterative method. In each iteration, the image vector to be reconstructed is multiplied by the similarity matrix, a procedure equivalent to shift-variant low-pass filtering. To suppress noise and image artifacts on the reconstructed image, the algorithm updates the reconstructed CT image by minimizing the total variation (TV) of the difference between the image and its filtered image under the data fidelity constraint. Note that, the proposed algorithm for the second CT scan does not regularize

on the TV of the image to be reconstructed as in the conventional TV based iterative CT reconstruction methods.[21, 22, 65, 67, 68, 72, 78] It is also distinct from other prior-image constrained iterative algorithms in that it does not rely on the matching of pixel values between the prior image and the image to be reconstructed. Instead, the improvement of reconstruction accuracy from reduced projections is based on an estimated classification of structures shared by the two images. The proposed iterative algorithm is therefore referred to as structure preserving iterative reconstruction (SPIR).

In this chapter, the DECT quality using SPIR is evaluated on both digital and physical phantoms. In particular, the effects of structure classification errors on SPIR and the limit of data reduction for satisfactory DECT accuracy are investigated. Reconstruction error, spatial resolution, noise level and error of measured electron density are used as the image quality metrics in these DECT studies.

2.2 Method

2.2.1 Formulation of SPIR framework

In the presented studies, a full-scan image is chosen to be reconstructed at high kVp using the standard FBP algorithm, and the reconstruction of a second sparse-view scan image at low kVp is aided by the structure preservation from the first CT image using SPIR. Similar to the optimization framework of other regularization-based iterative reconstruction algorithms,[33, 65, 79] the proposed SPIR method is formulated as the following constrained minimization:

$$\boldsymbol{\mu}_{\boldsymbol{L}}^{*} = \arg\min\left[\lambda \cdot R(\boldsymbol{\mu}_{\boldsymbol{L}}, \boldsymbol{\mu}_{\boldsymbol{H}}) + \frac{1}{2}\|M\boldsymbol{\mu}_{\boldsymbol{L}} - \boldsymbol{b}\|_2^2\right], s.t. \boldsymbol{\mu}_{\boldsymbol{L}}(i) \geq 0, \tag{2.1}$$

where $\boldsymbol{\mu_L}$ is the vectorized image at low kVp to be reconstructed, $\boldsymbol{\mu_H}$ is the vectorized image at high kVp reconstructed by FBP, $R(\boldsymbol{\mu_L}, \boldsymbol{\mu_H})$ is the regularization term quantifying the extent of structure preservation. M is the system matrix modeling CT forward projection, vector $\boldsymbol{b}$ is the measured line integrals, and $\left\|M\boldsymbol{\mu_L} - \boldsymbol{b}\right\|_2$ calculates the L-2 norm of the difference between the estimated and the raw projections, i.e., the data fidelity error. λ is a user-defined penalty weight, which balances structure preservation and reconstruction accuracy. Each element of $\boldsymbol{\mu_L}$, $\boldsymbol{\mu_L}(i)$, is constrained by image non-negativity.

The design of the regularization term $R(\boldsymbol{\mu_L}, \boldsymbol{\mu_H})$ is the key to the success of SPIR. The structural information is first extracted from the full-scan FBP image via a procedure that is referred as structure classification, which is inspired by the bilateral filtering method originated in the image processing field.[80] Bilateral filtering combines two types of image filtering, domain filtering and range filtering. The domain filtering suppresses image noise via weighted averaging with domain weights that decrease as spatial distance between two pixels increases. The range filtering is performed in the same way with range weights that decay with pixel value differences. In the structure classification of the new method, combined domain and range weights of bilateral filtering is used to quantify the similarity between any two pixels of the first full-scan CT image. These weights are organized in a matrix form and the bilateral filtering becomes similarity matrix multiplication.

In the implementation, the domain weight with respect to distance is set as a box function centered at 0 with a window size of X-by-X pixels, and the range weight with respect to the pixel value difference is set as a Gaussian function centered at 0 with a kernel

width h. The similarity between two pixels i and j, W_{ij}, on the full-scan CT image $\boldsymbol{\mu_H}$ is calculated by the following formula:

$$W_{ij}(\boldsymbol{\mu_H}, X, h) = \begin{cases} \dfrac{exp\left(-\frac{(\mu_H(i)-\mu_H(j))^2}{h^2}\right)}{\sum_{j\in\Omega_i^{(X)}} exp\left(-\frac{(\mu_H(i)-\mu_H(j))^2}{h^2}\right)} & j \in \Omega_i^{(X)} \\ 0 & otherwise \end{cases}, \tag{2.2}$$

where X and h are user-defined parameters, $\Omega_i^{(X)}$ is the X-by-X subset of the pixels in the neighborhood centered at pixel i. Note that the total similarity for one pixel is normalized to one.

To reduce errors of similarity calculation, a noise-suppressed $\boldsymbol{\mu_H}$ via bilateral filtering is first generated, i.e. multiplication by the similarity matrix W:

$$\widehat{\boldsymbol{\mu_H}} = W\boldsymbol{\mu_H}, \tag{2.3}$$

where each element of W is calculated using Eq. (2.2) with $X = 3$ pixels and $h = \sigma$, the noise standard deviation (STD) measured on a uniform area in $\boldsymbol{\mu_H}$. The similarity matrix W is then updated on the noise suppressed CT image $\widehat{\boldsymbol{\mu_H}}$ using Eq. (2.2) again (i.e., $\boldsymbol{\mu_H}$ is replaced by $\widehat{\boldsymbol{\mu_H}}$) with $h = \sigma$ and $X = 41$. In case that one pixel of interest does not have sufficient pixels with non-zero similarity, the window X is adaptively increased until the number of pixels with non-zero similarity exceeds 200 or the size of the search window equals that of the image.

The generation of similarity matrix W is a process of structure classification, because W contains the structural information of the image. For example, if the size of the

high energy image is N by N, the kth row of W, W_{ij}, $i = k, j = 1, 2, \ldots N^2$, can be reshaped as an N-by-N image, showing the relative similarity values of all pixels across the entire image compared with the kth pixel. In the new method, W is computed on the high-kVp CT image (hereafter is referred as W_H). Since the object structure remains unchanged in the low-kVp CT scan, the computed W_H is also an accurate estimate of the similarity matrix on the low-kVp CT image $\boldsymbol{\mu_L}$, W_L, i.e.:

$$W_H \approx W_L. \tag{2.4}$$

As a process of bilateral filtering in nature, multiplication of an image vector by an accurate similarity matrix W yields a noise or error suppressed image. The reconstructed low kVp image, $\boldsymbol{\mu_L}$, is expected to have a reduced quality due to insufficient projection data. As such, the similarity matrix calculated on $\boldsymbol{\mu_L}$ is inaccurate, and cannot be used to effectively reduce reconstruction errors. Therefore Eq. (2.4) is relied on for improved reconstruction of $\boldsymbol{\mu_L}$. If $\boldsymbol{\mu_L}$ is reconstructed accurately with low noise or small errors (e.g., from successful iterative reconstruction), multiplication of $\boldsymbol{\mu_L}$ by an accurately estimated similarity matrix (W_H based on Eq. (2.4)) should have small effects on $\boldsymbol{\mu_L}$, i.e.:

$$\boldsymbol{\mu_L} \approx W_H \boldsymbol{\mu_L}, \tag{2.5}$$

Eq. (2.5) is used as an additional data constraint in the design of the regularization term of the optimization framework. One may notice that the difference between $W_H\boldsymbol{\mu_L}$ and $\boldsymbol{\mu_L}$ is relatively large at structure edges. To better preserve edge signals, the regularization term $R(\boldsymbol{\mu_L}, \boldsymbol{\mu_H})$ is designed to be the TV of the difference of $W_H\boldsymbol{\mu_L}$ and $\boldsymbol{\mu_L}$ as:

$$R(\boldsymbol{\mu_L}, \boldsymbol{\mu_H}) = \frac{1}{2}\|\boldsymbol{\mu_L} - W_H\boldsymbol{\mu_L}\|_{TV} = \frac{1}{2}\|\nabla(A\boldsymbol{\mu_L})\|_1, \quad (2.6)$$

where $= I - W_H$, I is an identity matrix with the same size as that of W_H and $\|\cdot\|_1$ calculates the L1 norm. Note that, in Eq. (2.6), the matrix W_H is equivalent to a shift-variant low-pass filter computed from $\boldsymbol{\mu_H}$, thus $A = I - W_H$ is equivalent to a shift-variant high-pass filter. By plugging Eq. (2.6) into Eq. (2.1), one can reformulate the SPIR method as the following constrained minimization problem:

$$\boldsymbol{\mu_L^*} = \arg\min\left[\frac{\lambda}{2}\|\nabla(A\boldsymbol{\mu_L})\|_1 + \frac{1}{2}\left\|M\boldsymbol{\mu_L} - \vec{b}\right\|_2^2\right], s.t. \boldsymbol{\mu_L}(i) \geq 0. \quad (2.7)$$

The contribution of this algorithm development is mainly two-fold. First, this study reformulate bilateral filtering into similarity matrix multiplication, a form compatible with the framework of iterative CT reconstruction. Bilateral filtering, which is equivalent to shift-variant high-pass filtering, is included in the regularization term for improved CT reconstruction. Secondly, SPIR is developed to reduce the data acquisition of DECT since CT images at different energies on the same object share the same structures and therefore have almost identical similarity matrices. Only one high-quality CT image is needed to calculate an accurate similarity matrix, and thus the projection data of a second CT scan can be reduced and reconstruction errors can be suppressed by SPIR.

2.2.2 Implementation details of the SPIR algorithm

2.2.2.1 Summary of SPIR workflow

The DECT method using the SPIR algorithm implemented in this paper is summarized as follows:

1. Reconstruct a high kVp CT image $\boldsymbol{\mu_H}$ from a full scan using FBP reconstruction.
2. Generate noise-suppressed $\widehat{\boldsymbol{\mu_H}}$ by bilateral filtering via Eq. (2.2) and Eq. (2.3).
3. Calculate the similarity matrix W_H on $\widehat{\boldsymbol{\mu_H}}$ using Eq. (2.2).
4. Solve Eq. (2.7) and output $\boldsymbol{\mu_L}$.

2.2.2.2 Solver to Eq. (7)

To efficiently solve the constrained minimization problem, i.e., Eq. (2.7), a gradient projection with an adaptive Barzilai–Borwein (GP-BB) step-size selection scheme is used. The implementation is similar to that presented in Reference[22], except the gradient of the regularization term is included in the calculation of the descending direction of the objective function. Let $\boldsymbol{h} = A\boldsymbol{\mu_L}$, and the regularization term (Eq. (2.6)) can be rewritten as

$$R = \frac{1}{2}\|\nabla \boldsymbol{h}\|_1 = \frac{1}{2}\sum_{m,n}\sqrt{\left(h_{m,n} - h_{m,n-1}\right)^2 + \left(h_{m,n} - h_{m-1,n}\right)^2}, \tag{2.8}$$

where the vector $\vec{h}$ is reshaped as a $N_X \times N_Y$ image matrix whose elements are $h_{m,n}, 0 < m \leq N_X, 0 < n \leq N_Y$. $N_X \times N_Y$ is the image size of reconstruction. Similarly, $\boldsymbol{\mu_L}$ is reshaped as $\mu_{s,t}$ and A as $A_{m,n,s,t}$, $0 < s, m \leq N_X, 0 < t, n \leq N_Y$. Thus, $h_{m,n} = \sum_{s,t} A_{m,n,s,t}\mu_{s,t}$. Denoting the gradient of Eq. (2.8) with respect to $\boldsymbol{\mu_L}$ as $\vec{\nabla}R$, one can calculate its element via the following equation:

$$\left(\vec{\nabla}R\right)_{i,j} = \frac{\partial R}{\partial \mu_{i,j}} = \sum_{m,n} \frac{(h_{m,n}-h_{m,n-1})(A_{m,n,i,j}-A_{m,n-1,i,j})+(h_{m,n}-h_{m-1,n})(A_{m,n,i,j}-A_{m-1,n,i,j})}{\sqrt{(h_{m,n}-h_{m,n-1})^2+(h_{m,n}-h_{m-1,n})^2+\epsilon}}, \tag{2.9}$$

where ϵ is a small positive number to avoid singularities in the derivative calculation and is set as 10^{-8} in the algorithm.

ALGORITHM I shows the pseudo code of the solver of Eq. (2.7) by the GP-BB method. Line 1 lists algorithm parameters with typical values controlling the optimization. The penalty weight λ in the optimization objectives balances the strength of noise suppression and data fidelity error. The value of λ is empirically chosen to match the data fidelity error of the images with those of other methods for a fair comparison in the studies presented later. A typical value range is also given in Line 1. The initial guess of the low-kVp image in the optimization can be zero or generated by other iterative reconstruction algorithm (line 2). Note that, zero initial will give the same optimal solution but with more computation time. Line 3 to 16 is the main loop solving Eq. (2.7) using GP-BB method. When the L1 norm of the image difference between two adjacent iterations $\left\|\boldsymbol{\mu_L} - \boldsymbol{\mu_{L,old}}\right\|_1$ is less than the preset tolerance (line 15) or the number of iterations exceeds the upper limit N_{iter}, the iteration stops with a final result image $\boldsymbol{\mu_L}$ (line 17).

ALGORITHM I Pseudo code of solver to Eq. (2.7) by the GP-BB method (the comments are shown in italic).

1: $N_{iter} \coloneqq 2000$; $\kappa \coloneqq 0.3$; $tol \coloneqq 10^{-10}$; $\lambda \coloneqq 0.1\sim1$; *empirical control parameters*

2: $\boldsymbol{\mu_L} \coloneqq 0$ or result from other iterative reconstruction; *initial guess*

3: for $t \coloneqq 1: N_{iter}$ do *main loop*

4: $\boldsymbol{g} = \vec{\nabla} R + M^T(M\boldsymbol{\mu_L} - \boldsymbol{b})$; *gradient of objective function*

5: for $i \coloneqq 1{:}\,N$ do *enforce gradient negativity and projection non-negativity*

6: if $g(i) \leq 0$, or $\boldsymbol{\mu_L}(i) \geq 0$, then $p(i) \coloneqq g(i)$; else $p(i) \coloneqq 0$ end if;

7: end for;

8: if $t \coloneqq 1$, then

9: $\boldsymbol{\mu_{L,old}} \coloneqq 0$; $\boldsymbol{p_{old}} \coloneqq 0$; $\alpha \coloneqq 0$;

10: else *adaptive BB step size*

11: $\alpha^{BB1} \coloneqq \frac{(\boldsymbol{\mu_L} - \boldsymbol{\mu_{L,old}})^T(\boldsymbol{\mu_L} - \boldsymbol{\mu_{L,old}})}{(\boldsymbol{\mu_L} - \boldsymbol{\mu_{L,old}})^T(\boldsymbol{p} - \boldsymbol{p_{old}})}$, $\alpha^{BB2} \coloneqq \frac{(\boldsymbol{\mu_L} - \boldsymbol{\mu_{L,old}})^T(\boldsymbol{p} - \boldsymbol{p_{old}})}{(\boldsymbol{p} - \boldsymbol{p_{old}})^T(\boldsymbol{p} - \boldsymbol{p_{old}})}$;

if $\alpha^{BB2}/\alpha^{BB1} < \kappa$, then $\alpha \coloneqq \alpha^{BB2}$; else $\alpha \coloneqq \alpha^{BB1}$; end if;

12: $\boldsymbol{\mu_{L,old}} \coloneqq \boldsymbol{\mu_L}$, $\boldsymbol{p_{old}} \coloneqq \boldsymbol{p}$;

13: end if;

14: $\boldsymbol{\mu_L} \coloneqq \boldsymbol{\mu_L} - \alpha\boldsymbol{p}$; *update image*

15: if $\left\|\boldsymbol{\mu_L} - \boldsymbol{\mu_{L,old}}\right\|_1 < tol$, then break; end if; *stopping criterion*

16: end for;

17: return $\overrightarrow{f_L}$;

2.2.3 Evaluation

The feasibility of the proposed algorithm is demonstrated through both computer simulation and phantom experiments. In all the investigations, imaging parameters matching those of an On-Board Imager (OBI) cone-beam CT (CBCT) system on a Varian radiation therapy machine (e.g. Trilogy or Truebeam) are used, except that this study focuses on fan-beam CT studies to avoid scatter errors. Each projection contains 1024 pixels with a pixel pitch of 0.388 mm. A full scan over 360° acquires 655 projections. The

reconstructed CT images and the decomposed material images have a dimension of 512×512 with a pixel size of 0.5×0.5 mm^2. The CT images are converted to CT number in Hounsfield Unit (HU), and the decomposed material images are the relative weights (i.e., the effective volume fractions) of the basis materials. In simulation studies, a mono-energetic source at 47 keV and 61 keV is used. No scatter is simulated. Poisson noise is added on projections to simulate an image noise level close to that in experimental results. The phantom experiments are performed on the tabletop CBCT system at the Georgia Institute of Technology, with two x-ray tube energies of 75 kVp and 125 kVp. A fan-beam geometry with a longitudinal beam width of 15 mm on the detector is used to acquire views with scatter contamination inherently suppressed.[81] More details of the tabletop CBCT system can be found in Reference.[82]

High-energy CT images are reconstructed from raw data by the FBP method with a Hamming filter and are used for structure classification in SPIR. Low-energy CT images are reconstructed using SPIR with different numbers of equi-angular views. A practical reason of using a full high kVp scan and a sparse-view low kVp scan is that compared with the CT image of a full low kVp scan, the CT image of a full high kVp scan is less noisy in this study and thus can generate a more accurate similarity matrix. A more accurate similarity matrix leads to a high-quality CT image of the second sparse-view scan reconstructed by the new method. The decomposed material images are generated from high-energy and low-energy CT images by an iterative image-domain decomposition method recently developed.[83] CT images and decomposed material images by the conventional two-full-scan FBP method are used as the ground truth. The proposed algorithm is implemented in MATLAB. The majority of computation occurs in minimizing

the objective function of SPIR, which typically takes about 10 minutes on a 2.67GHz CPU. The generation of similarity matrix W takes about 20 seconds with 8-thread parallel computation.

The performance of the proposed DECT heavily relies on the accuracy of structure classification. To investigate DECT image qualities when structure classification is challenging, the algorithm is evaulated on a digital phantom with a water equivalent background containing 8 rods. On the high-energy CT image where structure classification is performed, the attenuation coefficients of the 8 contrast rods are carefully designed to assess the proposed SPIR-based DECT for the following three scenarios:

Scenario I: Rods have sufficient contrasts compared with the background and each rod has a different CT value and therefore is identified as a different material.

Scenario II: Rods have sufficient contrasts compared with the background but have the same CT values on the high-energy CT image. These rods may be therefore falsely classified as the same material although they have different CT values on the low-energy CT image.

Scenario III: Rods have no contrasts compared with the background on the high-energy CT image. Structure classification therefore completely fails.

Scenario I represents the most common situation on clinical DECT images. Scenario II may happen in some cases such as angiography bone removal when the intensities of iodine and bone partially overlap. Scenario III is an extremely challenging case for assessment purposes only. It is hypothesized that SPIR can accurately reconstruct

the image of rods in Scenario I with a high overall image quality, and may have lower accuracy in Scenario II and III depending on the number of views. In addition, one small rod with a diameter of 1cm that contains a 0.5cm calcium rod surrounded by iodine solution is included. Similar to scenario II, the two materials in this rod have the same pixel value in the high energy image but different pixel values in the low energy image. This rod is used to simulate the scenario in angiography that a vessel contains calcium plaque and iodine contrast with similar HU values in the high kVp image, and to evaluate the preservation of the calcium/iodine boundary in the reconstructed image by the new method.

The above studies focus on the evaluation of SPIR accuracy on the low-energy CT scan. The relative root-mean-square error (R-RMSE) is used as an image quality metric, which is calculated as

$$\text{R-RMSE} = \frac{\sqrt{\frac{1}{N}\sum_{i=1}^{N}(\mu_i - \mu_{i0})^2}}{\frac{1}{N}\sum_{i=1}^{N}\mu_{i0}} \times 100\%, \tag{2.10}$$

where i is the index of the region of interest (ROI), μ_i is the mean reconstructed CT value inside the ROI, μ_{i0} is the corresponding ground truth value, and N is the total number of the ROIs.

Measurements of line-spread function are used to evaluate the method performance on image spatial resolution. Besides rods, three 1-by-7-pixel lines with contrasts of 127 HU (line #1), 1017 HU (line #2) and 94 HU (line #3) corresponding to scenarios I, II and III, respectively, are added in the digital phantom to further study the performance of the proposed method. For each line, 7 1D profiles pass through all the 7 pixels at the direction perpendicular to the line and are averaged along the direction of the line. The averaged

profile is fitted by a Gaussian function and then converted to a modulation transfer function (MTF). The frequency at 10% of maximum value of MTF is used to quantify the MTF function, and is referred as "10% MTF frequency" for conciseness in the presentation of results. A larger value of 10% MTF frequency indicates a higher spatial resolution.

The overall performance of the proposed method is further evaluated on two physical phantoms, the Catphan©600 phantom and an anthropomorphic pediatric phantom. The slice of the line pairs on the Catphan phantom is used to investigate the spatial resolution. Both CT images and decomposed material images are generated. A uniform ROI in a CT image is also selected to measure the noise level. A similar study is performed on the anthropomorphic pediatric phantom to evaluate the method performance in the presence of complex object structures. A further evaluation is performed on head patient DECT images acquired at 140 kVp and 80 kVp. The full-scan CT image at 140 kVp is used for similarity matrix calculation. As the raw projection data on the clinical CT scanner is not accessible, the full-scan CT image at 80 kVp is forward-projected to generate a full-size sinogram. The projection views of the sinogram are then downsampled to simulate different sparse-view scans. This simulated sparse-view scan is reconstructed by the proposed method, and used in material decomposition of "iodine" and "tissue" images. This study focuses on the evaluation of virtual unenhanced imaging using DECT, a common clinical technique that removes iodine from contrast-enhanced DECT images and reduces the need for an unenhanced CT scan.[61] Virtual unenhanced images are generated by weighted summation of the decomposed images, in the same way as shown in Reference [62].

The contrast rod slice of the Catphan phantom is used to investigate the measurement accuracy of electron density using DECT, which is important in dose calculation for radiation therapy.[58] The electron density map is generated as the summation of the decomposed basis material images weighted by their known electron densities. Teflon and polystyrene are used as the two basis materials of which electron densities can be found in the phantom manual. The contrast rods are selected as the ROIs. The measurement error of electron density is calculated as:

$$E_i = \frac{\rho_i - \rho_{i0}}{\rho_{i0}} \times 100\%, \tag{2.11}$$

where ρ_i is the mean electron density of the *i*th ROI and ρ_{i0} is its ground truth obtained from the phantom manual. The absolute values of E_i of all ROIs are then averaged for comparison.

The above studies compare SPIR approach with the FBP method as well as a conventional TV regularization-based iterative reconstruction method (TVR), which uses the TV of the image to be reconstructed as the regularization term.[22, 84, 85]. On the digital phantom, the new approach is also compared with two iterative reconstruction methods: Prior Image Constrained Compressed Sensing (PICCS), a state-of-the-art algorithm that uses a prior image to improve the iterative CT reconstruction algorithm.[79] In PICCS, the strength parameter of prior image constraint is set as the value recommended in Reference [79] (i.e., $\alpha = 0.91$ in Eq.(3) of Reference [79]). In all the comparisons, the parameters of different algorithms are manually tuned to have the same data fidelity errors on the reconstructed images.

In particular, the method performance is assessed on DECT data of a full scan and a second scan with different numbers of projection views. For conciseness, the following abbreviations are used in the presentations of results. On the results of CT images, "Full-scan FBP" stands for the FBP reconstruction using a full scan dataset, "*N*-view SPIR/TVR/PICCS" stands for reconstruction by SPIR, TVR or PICCS using data of *N* views, and "high E/low E" stands for high energy CT image or low energy CT image. On the results of decomposed material images, electron density maps and virtual unenhanced images, "Full+Full FBP" refers to the conventional two-full-scan FBP method, and "Full+*N* SPIR" refers to the proposed DECT method using one full-scan FBP image and a second *N*-view SPIR image.

2.3 Results

2.3.1 Digital phantom study

Figure 2.1 shows the digital phantom setting at low energy and high energy. Both images are reconstructed by full-scan FBP as the ground truth. Figure 2.2 shows the CT images of the digital phantom reconstructed by SPIR, TVR and PICCS with a sparse-view scan at the low energy level. In the comparison of TVR and PICCS with SPIR results, the algorithm parameters is tuned to achieve the same data fidelity errors. The parameter α in PICCS, i.e., the strength of prior image constraint, is set as 0.91, the recommended value in Reference [79].

From Figure 2.2, it is seen that TVR and SPIR have similar reconstruction accuracy on a 50-view scan. The advantage of SPIR becomes prominent as the number of views further decreases. The images of SPIR on scans with 20 and 10 views show fewer patchy

artifacts than those by TVR (see Figure 2.2(a2), (a3), (b2) and (b3)). This finding is consistent with the measured reconstruction accuracies of CT numbers listed in Table 2-I. SPIR with a 10-view scan has an R-RMSE of 1.33%, while TVR introduces large errors with the same number of views and increases R-RMSE to 6.18%. The CT images of SPIR show sharper edges for rods with sufficient contrast in the high-quality CT image of the first scan (i.e., the scenario I and II rods) than the TVR images, which indicates a better spatial resolution on these objects. The result of PICCS shows a comparable accuracy and spatial resolution with that of SPIR, while it is much noisier. On the zoomed-in ROI of "vessel" simulating calcium plaque and iodine contrast which have the same pixel values in the high energy image, the boundaries between calcium and iodine are preserved in the low energy images of SPIR with scans of 20 views or more, a similar performance compared with TVR and PICCS (see Figure 2.2(a2), (b2) and (c2)). However, TVR and PICCS fail to maintain the vessel shape, mainly because of their poor reconstruction accuracy for such a small object. On the scenario III rods with no sufficient contrast in the CT image of the first scan, the structure classification fails in SPIR. However, SPIR still achieves similar image qualities with 10 views as TVR and PICCS. It is worth emphasizing again that scenario III represents the most challenging case for SPIR and is considered rare in clinical practice.

The measured 10% MTF frequency and noise STD are listed in Table 2-II. On both line #1 and line #2 (i.e., scenario I and II, respectively), SPIR outperforms TVR on spatial resolution with the 10% MTF frequency higher by an average factor of 4, and maintains a similar noise STD. SPIR and PICCS show similar spatial resolutions indicated by similar 10% MTF frequency. However, SPIR outperforms PICCS on noise suppression with a

noise STD lower by a factor of 7. On line #3 (i.e., scenario III), SPIR, TVR and PICCS all fail to show observable contrast for this line. The above study reveals that the proposed SPIR is superior to TVR on spatial resolution with similar noise suppression, and superior to PICCS on noise reduction with similar spatial resolution.

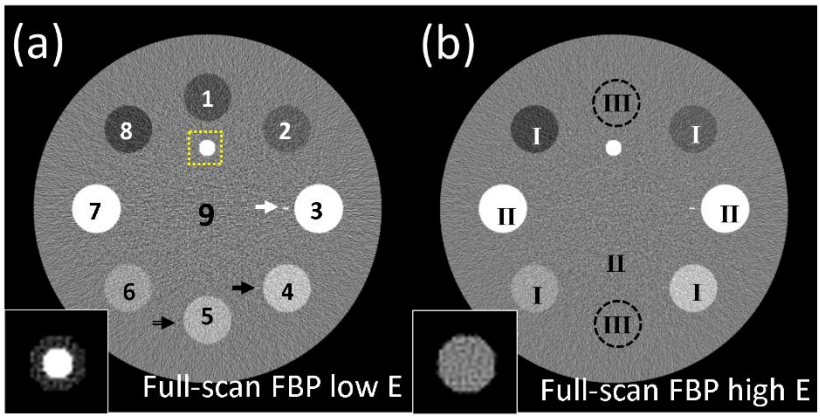

Figure 2.1 CT images of a digital phantom reconstructed by full-scan FBP reconstructions at (a) low energy level, (b) high energy level. The labels in (a) are the indices of ROIs, and the labels in (b) indicate the different scenarios for each ROI. The dashed-line square in (a) indicates the region where the zoomed-in "vessel" at the bottom-left of each image is located. The black arrow, white arrow and double line arrow in (a) show the positions of line #1, line #2 and line #3 (corresponding to scenario I, II and III, respectively). Display window for full-FOV images is [-250 250] HU, and for zoomed-in "vessel" at bottom-left is [$\overline{HU}$-80 $\overline{HU}$+80] HU, where $\overline{HU}$ is the mean HU value of the "vessel" in each case.

Table 2-I Measured CT number (in HU) of the ROIs and the background on CT images shown in Figure 2.1. The indices of ROIs are marked in Figure 2.1(a). The indices of scenarios are marked in Figure 2.1(b). The R-RMSEs are calculated by Eq. (2.10) with the ground truth obtained from the full-scan FBP images. The proposed SPIR method and TVR are applied on low-energy CT scans with different numbers of views. Note that, although the contrast rods have different linear attenuation coefficients at two different x-ray energies, their CT numbers in HU may be similar on the CT images of the two scans.

	ROI	Ground truth	Low-E CT via SPIR			Low-E CT via TVR		
# of views		N/A	50	20	10	50	20	10
Scenario I	2	-58	-59	-60	-61	-59	-60	-46
	4	127	127	127	125	128	128	114
	6	63	63	63	65	63	61	51
	8	-112	-114	-114	-114	-114	-112	-95
II	3	1017	1017	1016	1015	1018	1016	1004
	7	850	850	849	847	851	850	836
III	1	-87	-88	-87	-83	-87	-85	-69
	5	94	96	96	92	95	95	87
Background	9	0	0	0	4	0	0	6
R-RMSE (%)			0.50	0.60	1.33	0.48	0.61	6.18

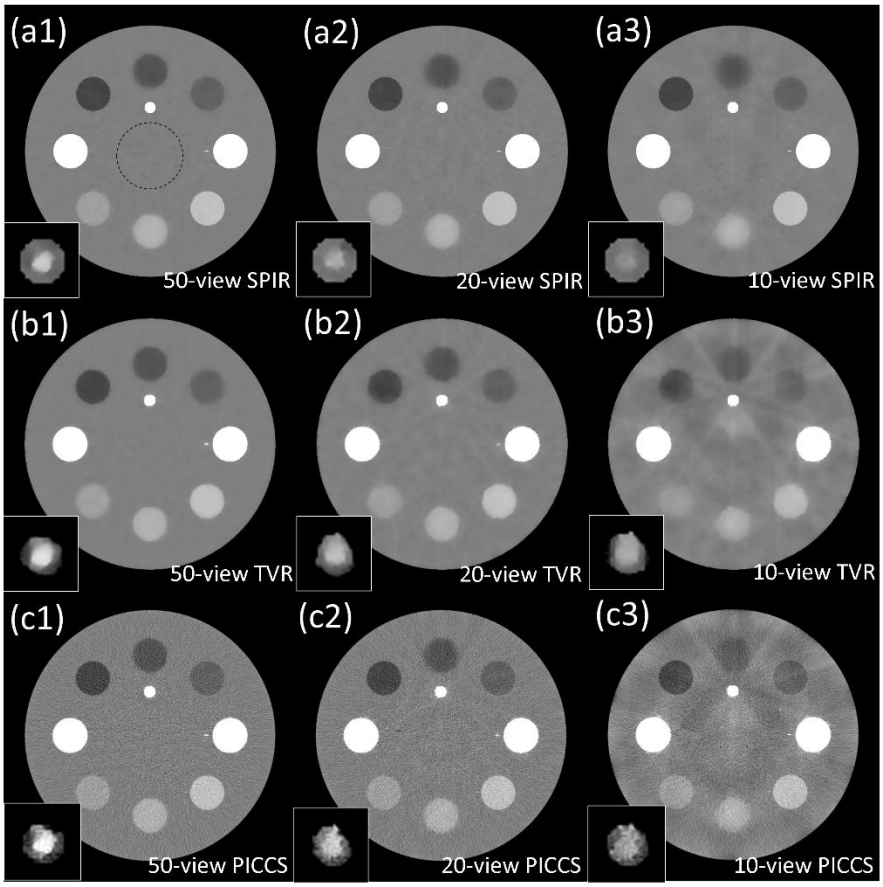

Figure 2.2 CT images of a digital phantom at low energy reconstructed by (a) SPIR, (b) TVR and (c) PICCS using (1) 50 views, (2) 20 views and (3) 10 views. The zoomed-in "vessel" at the bottom-left of each image is indicated by the dashed-line square in Figure 2.1(a). The dashed circle shown in (c) is the ROI on which the noise STD in Table 2-II is calculated. Display window for full-FOV images is [-250 250] HU, and for zoomed-in "vessel" at bottom-left is [$\overline{HU}$-80 $\overline{HU}$+80] HU, where $\overline{HU}$ is the mean HU value of the "vessel" in each case.

Table 2-II 10% MTF frequency values and noise STD measured on Figure 2.2.

	10% MTF frequency (lp/mm)					
	50-view scan		20-view scan		Average	Noise STD (HU)
	Line #1	Line #2	Line #1	Line #2		
SPIR	13.90	8.80	15.20	8.34	11.56	5
TVR	3.31	2.90	1.77	2.97	2.74	5
PICCS	6.76	11.43	6.29	11.48	8.99	34

2.3.2 Catphan phantom study

Figure 2.3 shows the CT images of the Catphan phantom on the slice of line pairs, reconstructed by FBP, TVR and SPIR. The dotted circle area in Figure 2.3(c) is selected as the ROI, of which the means and noise STDs are measured in Table 2-III. SPIR achieves noise STD reduction by a factor of more than 10 compared with the full-scan FBP reconstruction. With the same data fidelity error, SPIR substantially outperforms the TVR method on image spatial resolution with half of the noise STD. As shown in the zoomed-in insert of each image on the ROI (indicated by the white rectangle in Figure 2.3(a)), the TVR method has a spatial resolution of less than 5 pairs/cm when the view number is 50 (see Figure 2.3(f)), while SPIR on even 10 views (see Figure 2.3(e)) has a spatial resolution of 6 pairs/cm, comparable to that of the full-scan FBP image. The corresponding DECT decomposed images are shown in Figure 2.4. The aluminum (the line-pair material) and the epoxy (the background) are chosen as the basis materials. It is seen that the high quality

of CT images reconstructed by SPIR leads to high spatial resolution on the decomposed images.

One may notice some low frequency artifacts in the decomposed images shown in Figure 2.4(d2). Compared with simulation studies, phantom experiments contain larger projection errors mainly from beam-hardening and scatter. These errors propagate through both reconstruction and decomposition processes. In reconstruction, because of the very limited number of views in one scan, the error is non-uniformly distributed across the reconstructed image. This artifact is not obvious in the CT images, but it is magnified and becomes noticeable after material decomposition, which is an error-sensitive process. [83]

A different slice of contrast rods of the Catphan phantom is used to evaluate the electron density measurement accuracy of SPIR-based DECT. Figure 2.5 shows the electron density maps generated by the conventional two-full-scan FBP and SPIR-based DECT. The measurement errors of ROIs are listed in Table 2-IV. The average errors on the results by SPIR-based DECT are comparable with those of the conventional two-full-scan FBP, which indicates the high accuracy of the decomposed images and electron density maps obtained by the new method. As a side note, the measurement errors of electron densities shown in Table IV are different from those reported in the recent papers.[33, 83] It is mainly because of the different basis materials used in the DECT decomposition as well as the different phantom geometry.

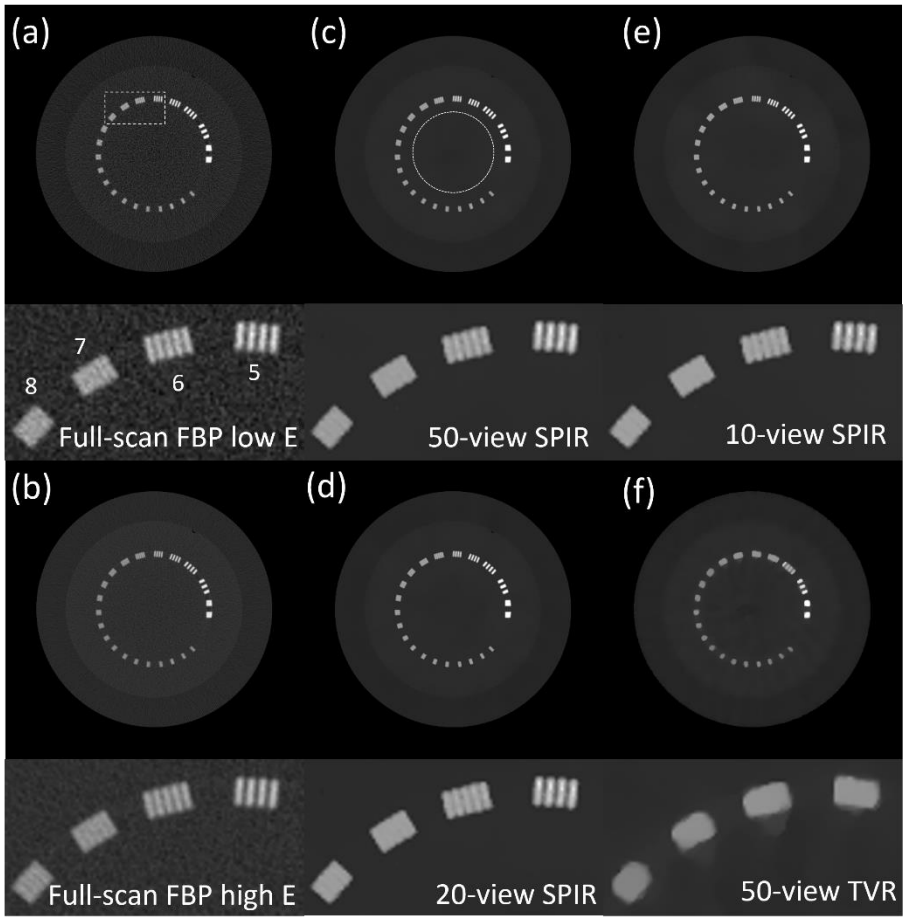

Figure 2.3 CT images of the Catphan phantom on the slice of resolution line pairs, reconstructed by FBP on full scan data at (a) low kVp and (b) high kVp, SPIR at low kVp using (c) 50 views, (d) 20 views and (e) 10 views, and (6) TVR at low kVp using 50 views. The dashed rectangle shown in (a) is the region where the zoom-in inserts of line pairs are located. The dotted circle shown in (c) is the ROI on which Table 2-III is calculated. Labels in the bottom figure of (a) show the value of line pairs per cm for each line cluster. Display window: [-500 2500] HU.

Table 2-III The means and the noise STDs of the CT number (in HU) in the ROIs indicated by the dotted circle shown in Figure 2.3(c).

Methods	Mean ± STD
Full scan FBP at 75kVp	-4±128
Full scan FBP at 125kVp	60±62
50-view SPIR at 75kVp	-4±9
20-view SPIR at 75kVp	-7±6
10-view SPIR at 75kVp	-4±7
50-view TVR at 75 kVp	-4±16

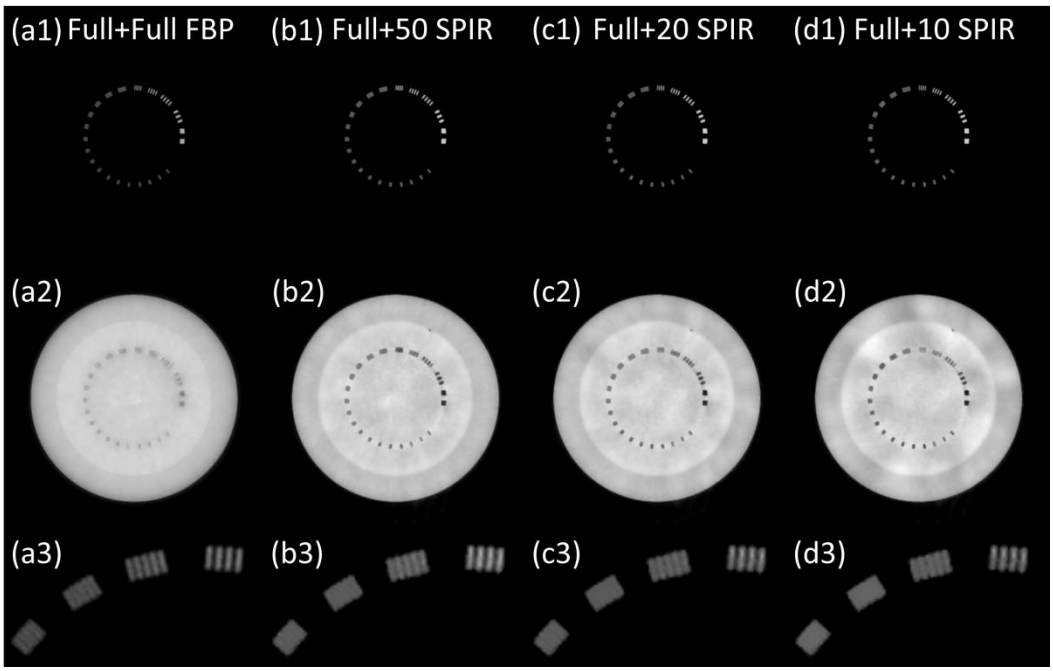

Figure 2.4 The decomposed material images of line pair slice, based on the reconstruction images at low kVp and high kVp using (a) conventional two-full-scan FBP, SPIR-based DECT using one full scan and a second (b) 50-view, (c) 20-view and (d) 10-view scan. Row (1): "bone" images; row (2): "tissue" images; and row (3): magnified views of bone images in the ROI of dashed rectangle in Figure 2.5(a). Display window: [0.1, 1.2].

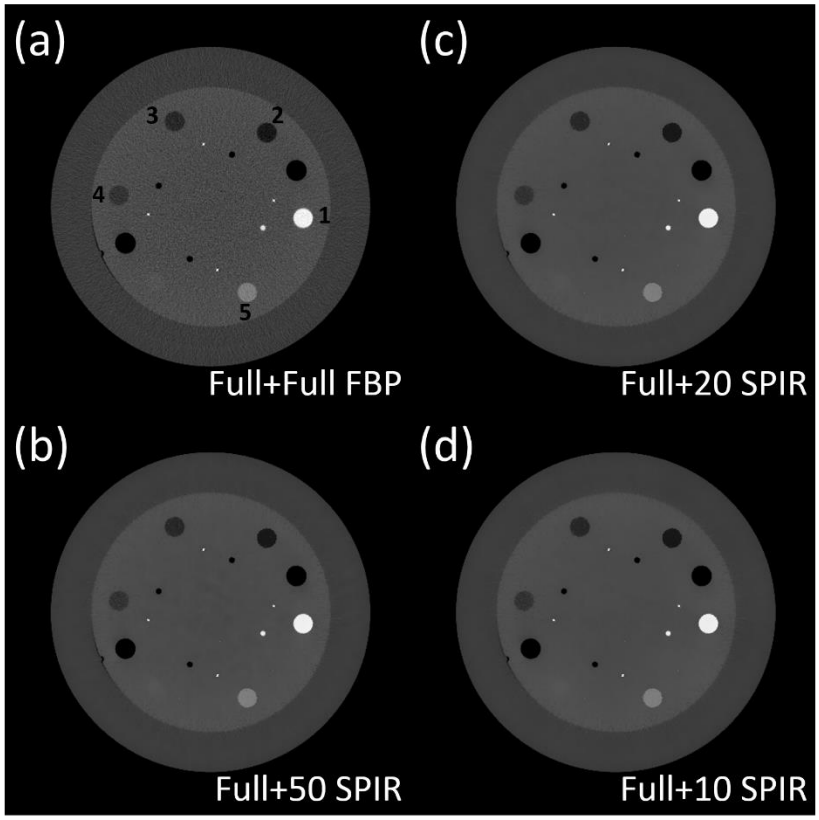

Figure 2.5 Electron density maps of contrast rods, based on the reconstruction images at low kVp and high kVp using (a) conventional two-full-scan FBP, SPIR-based DECT using one full scan and a second (b) 50-view, (c) 20-view and (d) 10-view scan. The labels in (a) indicate the ROIs on which Table IV is calculated. Display window: [2.5 6.5]$\times 10^{-23}$ cm^{-3}.

Table 2-IV The percentage error of electron density measurement of contrast rods using conventional two-full-scan FBP and SPIR-based DECT with one full scan and a second N-view scan ("Full+ N"). The indices of the ROIs are marked in Figure 2.5(a). The ground-truth electron density values are obtained from Catphan©600 phantom manual. The average absolute error is the average of the absolute values of error in all ROIs.

Scan scheme	1 Teflon	2 PMP	3 LDPE	4 Polystyrene	5 Delrin	Average absolute error
Conventional two-full scan FBP	0.64%	0.81%	-0.63%	-0.45%	-1.69%	0.84%
Full+Full	0.48%	0.95%	-0.60%	-0.18%	-1.71%	0.78%
Full+50	0.32%	0.98%	-0.57%	-0.75%	-1.65%	0.85%
Full+20	0.16%	1.01%	-0.57%	-0.95%	-1.80%	0.90%
Full+10	-0.18%	0.60%	-1.24%	-0.88%	-1.65%	0.91%

2.3.3 Pediatric phantom study

An anthropomorphic pediatric phantom with realistic vertebra structures is used to evaluate the performance of the new method on objects with a complex geometry. The bone of the phantom is made of calcium and the soft tissue is composed of epoxy. Figure 2.6 and Figure 2.7 show the CT images and decomposed material images. Similar to previous results, SPIR-based DECT generates accurate CT images and decomposed images with clearly separated bone and tissue structures. The error maps of CT image reconstructed by SPIR are shown in Figure 2.6(c), with the full-scan FBP image considered as the ground truth. Three rectangles indicated by the dashed rectangle in Figure 2.6(a1) are used as the ROIs for the measurement of the root-mean-square-error (RMSE) in HU, shown in Table 2-V. Overall, SPIR maintains a low reconstruction error of less than 10 HU

for scans with different numbers of views, except for the 10-view scan where the RMSE increases to 18 HU. A similar performance on image qualities for different numbers of views is observed on decomposed images shown in Figure 2.7. Similar low frequency artifacts are also shown in Figure 2.7(e2) as those of Figure 2.4(d2). These artifacts stem from the reconstruction error shown in Figure 2.6(c), which is magnified in the error-prone procedure of material decomposition.[83]

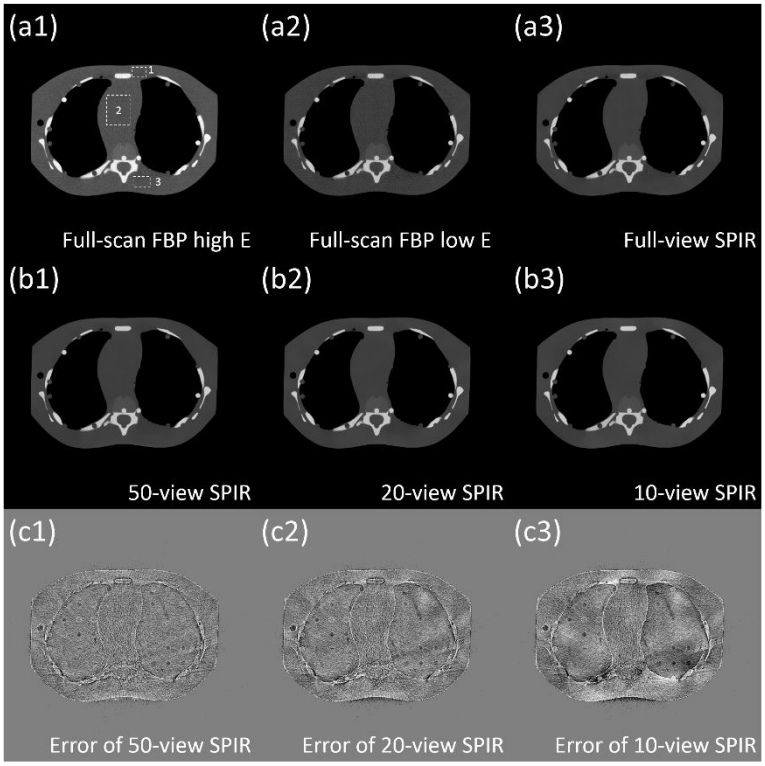

Figure 2.6 CT images of the pediatric phantom, reconstructed by full-view scan using (a1) FBP at high kVp, (a2) FBP at low kVp and (a3) SPIR at low kVp, and SPIR at low kVp using (b1) 50 views, (b2) 20 views and (b3) 10 views. The error maps of SPIR using (c1) 50 views, (c2) 20 views and (c3) 10 views compared with the full-scan FBP are also shown. The dashed rectangles in (a1) are the ROIs on which Table 2-V is calculated. Display window is [-500 1500] HU for (a) and (b), and is [-150 150] HU for (c).

Table 2-V Measurements on error of mean pixel value and RMSE (both in HU) on CT images reconstructed by SPIR with different numbers of views. The ROIs are marked in Figure 2.6(a1). The CT image of full-scan FBP at low kVp is chosen as the ground truth.

Number of views	Error of mean HU			RMSE
	ROI 1	ROI 2	ROI 3	
655	5	-1	2	3
50	13	0	8	9
20	10	2	8	7
10	14	0	28	18

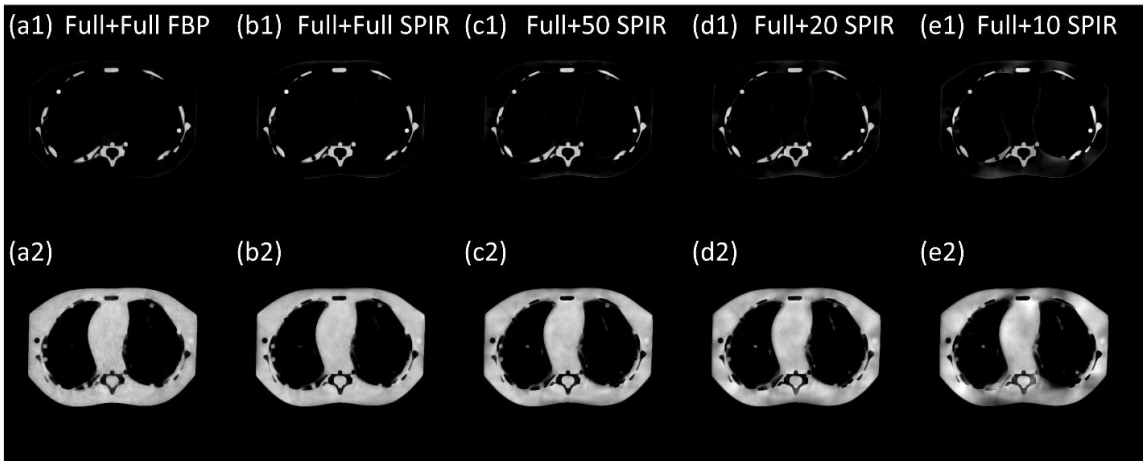

Figure 2.7 The decomposed material images of the pediatric phantom, based on the reconstruction images at low kVp and high kVp using (a) the conventional two-full-scan FBP, the proposed SPIR-based DECT using one full scan and a second scan with (b) full views, (c) 50 views, (d) 20 views and (e) 10 views. Row (1) is the "bone" image and row (2) is the "tissue" image. Display window: [0.1 1.2].

2.3.4 Clinical study

Head patient DECT images acquired at 140 kVp and 80 kVp with full scans are used to further evaluate the performance of SPIR on a clinical dataset. Figure 2.8 and Figure 2.9 show the CT images and the virtual unenhanced images, with a narrow display window of 80 HU. To quantify the reconstruction accuracy by SPIR, RMSEs are measured on CT images in three uniform ROIs indicated by the dashed rectangles in Figure 2.8(a1). The maximum RMSE is 7.2 HU when SPIR uses a second scan of only 10 views. As the number of projection views reduces, image non-uniformity and artifacts increase on the SPIR results. However, in the virtual unenhanced images of Figure 2.9, it is seen that the vessels containing iodine contrast agency are successfully removed in the results using SPIR reconstructions on even 20 views, with an image quality similar to that using full-scan FBP.

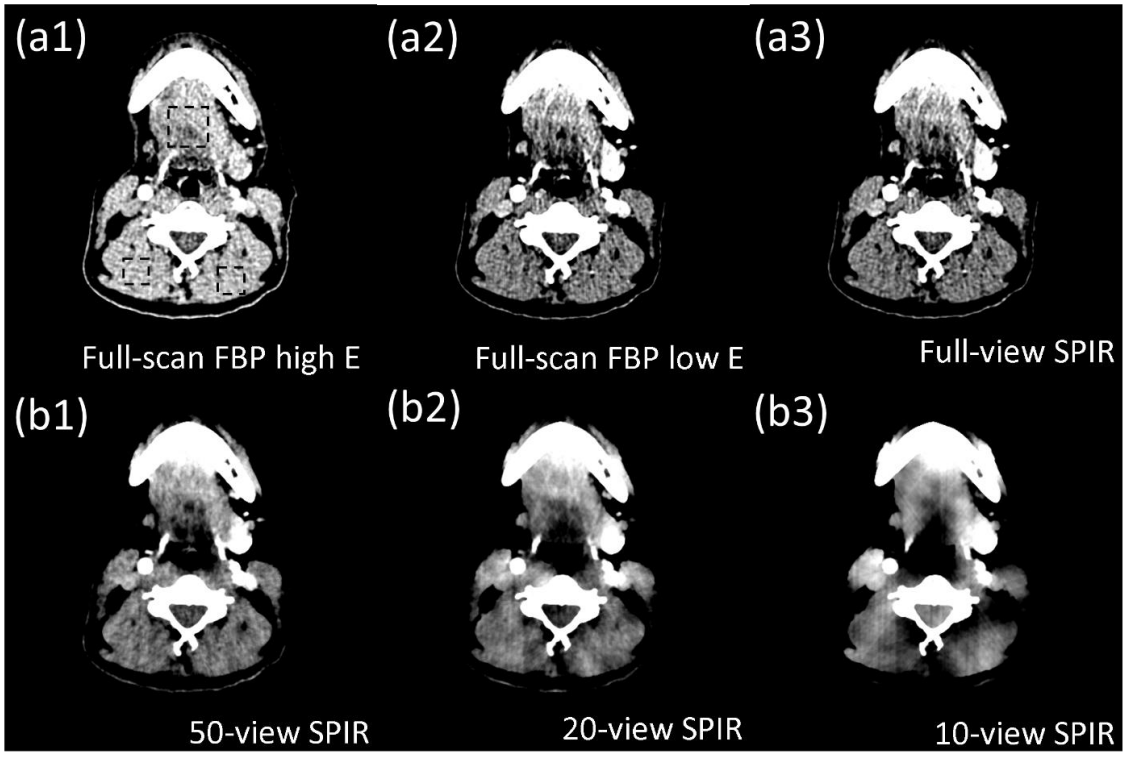

Figure 2.8 CT images of a head patient, reconstructed by (a1) full-view FBP at high kVp, (a2) full-view FBP at low kVp, (a3) full-view SPIR at low kVp, and SPIR at low kVp using (b1) 50 views, (b2) 20 views and (b3) 10 views. The dashed rectangles in (a1) are the ROIs on which RMSE is calculated. Display window is [0 80] HU.

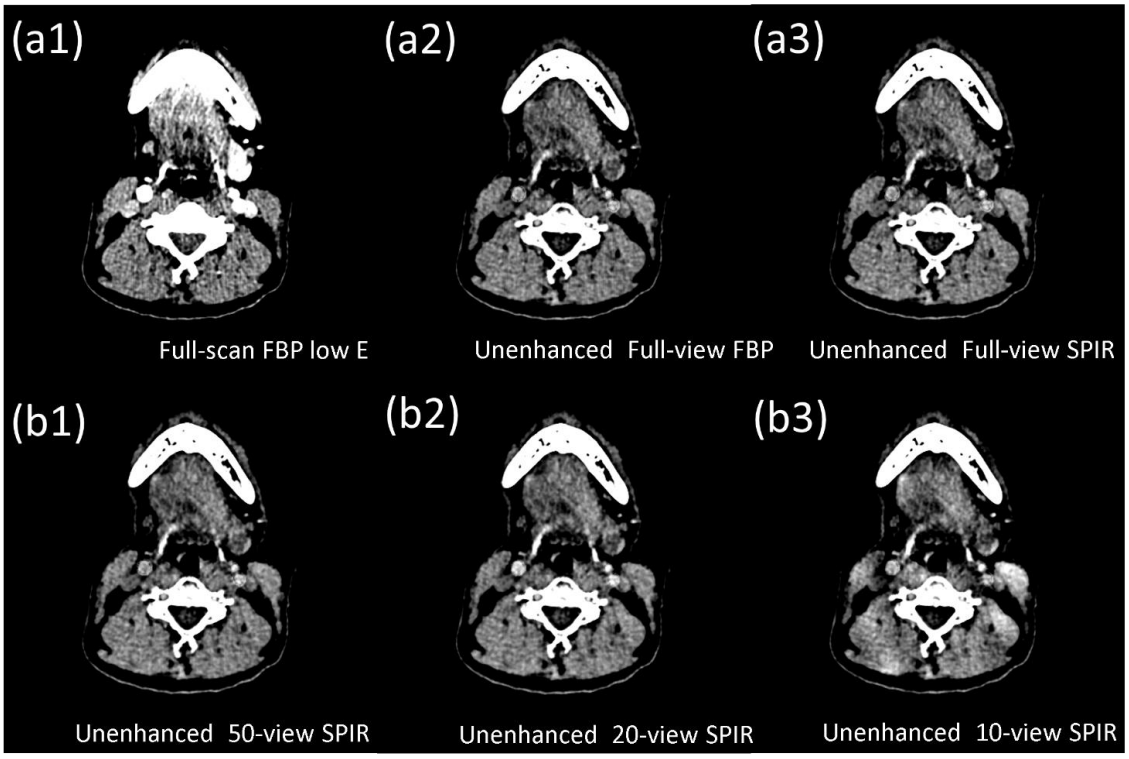

Figure 2.9 The original CT image and the virtual unenhanced CT images of a head patient. The virtual unenhanced CT images are generated from decomposed soft tissue and iodine images using (a2) the conventional two-full-scan FBP, the proposed SPIR-based DECT with one full scan and a second scan of (a3) full views, (b1) 50 views, (b2) 20 views and (b3) 10 views. The contrast-enhanced full-scan FBP image at low kVp is shown in (a1) for reference. Display window is [0 80] HU.

2.4 Conclusions and discussion

This work developed a new iterative CT reconstruction algorithm, SPIR, to reduce the data requirement for DECT. On a digital phantom, SPIR reduces the number of views in the second scan of DECT to as low as 10 with a reconstruction error of less than 1.5%. On physical phantoms, in addition to reduction of data acquisition in the second scan down to tens of views, SPIR achieves the same spatial resolution and an average error of less than 20 HU compared to the CT image reconstructed by the full-view FBP with image noise STD one order of magnitude less. Comparisons show that SPIR substantially

improves over TVR on the reconstruction accuracy of a 10-view scan by decreasing the reconstruction error from 6.18% to 1.33%. SPIR also outperforms TVR at 50-view and 20-view scan in image spatial resolution with a higher 10% MTF frequency by an average factor of 4. Compared with the results by PICCS in 50-view and 20-view scan, the image reconstructed by SPIR has similar spatial resolution but with a noise STD 7 times lower. The high accuracy of SPIR leads to the high spatial resolution of decomposed material images and the high accuracy of electron density maps. The electron density map obtained from the SPIR-based DECT images with a second 10-view scan has an average error of less than 1%.

The performance of SPIR is demonstrated using a rotation-rotation mode of the broad-sense DECT technique with linear image-domain decomposition. Compared with the non-linear projection-domain decomposition of DECT in its original concept, such an implementation simplifies the signal processing of DECT at the price of lacking beam-hardening correction capability.[36] It should be noted, however, that the research presented in this study is focused on the design of a new reconstruction algorithm for DECT independently of the decomposition process, and the use of SPIR does not require an image-domain decomposition. For example, a non-linear decomposition can be first performed on the dual-energy projection data using the same method as shown in recent publication,[86] and then carry out SPIR on the decomposed projections.

This study primarily focuses on the development of a new reconstruction framework that reduces data acquisition for DECT without much degradation of image quality. The presented proof-of-concept studies choose to evaluate the method performance using a rotation-rotation scan mode. It should be noted, however, that the rotation-rotation

scan mode is not an ideal scheme of DECT imaging for the new method in clinical use. The involuntary patient movement might comprise the assumption that the second CT scan of DECT contains the same structural information as the first CT scan. The performance of the proposed algorithm is therefore expected to be more robust on advanced DECT scanners,[39, 41] where patient motion is minimized via acquisition of dual-energy projections in a single scan.

This chapter describes a new reconstruction framework that reduces data acquisition for DECT without much degradation of image quality. By reducing data acquisition for DECT, SPIR can potentially reduce radiation dose on patients and hardware costs of the imaging system. For example, a "fast kVp switching" CT scanner [39] acquires dual-energy projections in one single rotation via switching the x-ray energy for neighboring projections. Since data acquisition is doubled without increasing scan time, the scanner is equipped with a fast detector and a fast-switching high-voltage generator, both of which significantly increase the system cost. The small number of projections in the low-kVp scan enabled by the new method indicates that the switching rate can be significantly lowered on the kVp-switching CT scanner. A fast detector also becomes unnecessary as the total number of DECT projections only slightly increases compared with that of a single-energy CT scan. The manufacturing cost can therefore be substantially reduced on such a "slow kVp switching" DECT system.[34] On a dual source CT,[41] The second sparse-view scan used by the proposed algorithm potentially leads to dose reduction on DECT imaging. In this paper, it have shown that a second scan with only 20 views (3% of a full scan, and thus negligible imaging dose) is sufficient for DECT imaging with a satisfactory image quality. In a clinical DECT protocol, it has been reported that, in order

to maximize CNR, the optimal dose ratio between the low- and high-energy scans is approximately 1:2.[87-89] It is therefore roughly estimated that the dose reduction achieved by the proposed method is about 30%, compared with the dose of DECT using two full scans. A thorough evaluation of dose reduction, however, entails comprehensive studies for different image quality metrics, clinical tasks and disease sites, and it is considered beyond the scope of this work.

The parameters in similarity matrix generation are empirically chosen to yield results with satisfactory qualities. In the step of bilateral filtering for noise suppression, a small size of spatial window (i.e., $X = 3$) is used to ensure that each pixel is locally averaged by its neighboring pixels. In the step of similarity calculation step, a large window (i.e., $X = 41$) is used such that each pixel has a large number of pixels for similarity calculation. An over-large window includes too distant pixels that are less likely to be the same material, and also dramatically increases the memory burden. If the found similar pixels are less than a threshold value (200 in the presented implementations), the window size is adaptively enlarged until the threshold value is met. Otherwise the pixels with few similar pixels are less regularized and tend to be reconstructed poorly. In this paper, it is found that the results obtained by the proposed algorithm are not sensitive to the above parameter values. As such, these parameters are fixed in all presented studies on different phantom data. For fair comparisons of SPIR, TVR and PICCS, the regularization weighting of different algorithms are manually tuned to have the same data fidelity errors on the reconstructed images. Readers may notice that the results of TVR (see Figure 2.1(c), (e), (g) and 6(f)) appear over-smoothed. It is because the data fidelity error is too large for

TVR, while the same data fidelity error enables the new method to achieve a very high image quality with significantly reduced noise.

The success of SPIR mainly stems from the establishment of an additional data constraint shown in Eq. (2.5), where a similarity matrix W is used to exploit the redundant structural information of the CT images of the same object acquired at two different energies. By enforcing the new data constraint during the iterative reconstruction, SPIR shows promise on more accurate CT construction than TVR, a popular algorithm of iterative CT reconstruction. Studies have shown that TVR could over-smooth CT images and generate contouring artifacts because of its tendency to penalize the image gradient irrespective of the image structures.[72, 78, 90, 91] Instead of reducing signal variations only on adjacent pixels as done in TVR, SPIR reduces signal variations for all pixels of the same structure, which effectively avoids the image artifacts of a TVR reconstruction. As SPIR adopts an optimization framework with regularization, it is also possible to combine SPIR with TVR for unified benefits of these two algorithms.

CHAPTER 3. PIXEL-WISE ESTIMATION OF NOISE STATISTICS ON ITERATIVE CT RECONSTRUCTION FROM A SINGLE SCAN

3.1 Introduction

Computed tomography (CT) imaging dose becomes an increasing public concern nowadays.[92] Iterative reconstruction algorithms have shown promise on improving quality of CT images reconstructed from projection data with reduced radiation.[28] To provide an evaluation tool for clinical utility of iterative CT reconstruction, this chapter describes a practical method for pixel-wise estimation of noise statistics on iteratively reconstructed CT images from a single scan.

Excessive CT dose can lead to the increased risks of radiation-induced cancer and genetic defects.[5, 6] CT dose can be lowered by optimizing data acquisition protocols (e.g. automatic exposure control),[8] improving detector designs,[9] using reconstruction from reduced projections,[93] or applying noise suppression methods with degraded spatial resolution.[15] After continuous optimization of CT systems for decades, further dose reduction from these techniques is expected to be limited or costly. By modeling the physical process of a CT scan and incorporating prior knowledge, iterative CT reconstruction algorithms are more resistant to noise and therefore require less imaging dose for the same image quality, compared with standard analytical CT reconstruction. Despite the increasing number of publications on iterative CT reconstruction,[22, 28, 29] little research has been devoted to studies on noise statistical properties of these algorithms.

A statistical analysis of CT image noise usually involves measurements of noise standard deviation (STD) and noise power spectrum (NPS). Noise STD quantifies the uncertainty level of pixel values, and is related to a wide range of image quality matrices such as signal-to-noise ratio. NPS describes the noise correlation among neighboring pixels and determines the noise texture of CT images.[30] As low-dose imaging protocols using iterative algorithms becomes more popular, a practical algorithm of noise STD map and NPS calculation on an iteratively reconstructed CT image could be a useful complementary tool in clinical practice. For example, an accurately measured noise STD map provides radiologists a reference map of reconstruction uncertainty during the diagnosis process. The NPS analysis aids radiologists to optimize the parameters of iterative reconstruction algorithm for a preferred noise texture. Moreover, the comparison of noise STD and NPS for different iterative reconstruction algorithms may help imagers choose the most suitable reconstruction method for a specific clinical task.

Accurate noise STD or NPS measurements require multiple scans on the same object without changing scan settings, which is considered impractical in clinical CT imaging. To estimate image noise statistics from a single CT scan, a commonly used method is to select a uniform region of interest (ROI) on the CT image, and then measure noise STD and NPS on the ROI, treating all the image pixels as random samples of the same probability distribution. This method inevitably lowers the spatial resolution of a STD map since a large size of ROI is needed for accurate noise measurement. Furthermore, it is implicitly assumed that all image pixels of the ROI obey the same signal statistics. This assumption is inaccurate on a clinical image since the selected ROI does not always have

uniform mean values and the noise level and spatial correlation vary across the entire image.

A more elegant approach for estimation of noise statistics on a CT image is to directly compute noise STD at each pixel or NPS on a CT image from the raw projection data. For example, an analytical algorithm with a filtered-backprojection (FBP) structure can be used to reconstruct the noise STD map on a CT image obtained by a standard FBP reconstruction method.[94] The theories of noise propagation from raw projection data to an iteratively reconstructed CT image have been previously developed, and can be divided into two main categories: propagation-based methods[95-97] and fixed-point based methods[98-100]. However, most existing methods are limited to the iterative CT reconstruction algorithms with quadratic regularization terms. As numerous non-quadratic regularization terms with better reconstruction properties have been proposed to improve iterative CT reconstruction,[79, 101, 102] it is of great importance to develop a practical method of computing the pixel-wise noise statistics for general iterative reconstruction methods.

This chapter describes a general method for estimating the pixel-wise noise statistics of iteratively reconstructed CT images from a single scan. The method is based on the noise propagation from the projection data through the reconstruction process, and a practical algorithm is then developed to compute the pixel-wise noise statistics (i.e., noise STD and NPS). The accuracy of this new method is evaluated on an anthropomorphic phantom via comparisons with the ground truth obtained from repeated CT scans. The clinical utility of the new approach is demonstrated by implementations on a set of head and neck patient CT data.

3.2 Method

3.2.1 Noise propagation in iterative CT reconstruction

The primary goal is to develop a practical algorithm of calculating noise distributions on CT images generated by existing iterative CT reconstruction techniques. This chapter studies iterative CT algorithms that can be written in the form of regularization-based optimization (shown below as Eq. (3.1)), a well-established framework used by different research groups.[22, 29, 101] Note that, another group of compressed sensing (CS) based algorithms, where data fidelity is used as an optimization constraint, can be converted to Eq. (1) as shown in Reference.[21].

$$\widehat{\boldsymbol{\mu}} = \arg\min f(\boldsymbol{\mu}) = \arg\min_{\boldsymbol{\mu}} \left[\frac{1}{2}(M\boldsymbol{\mu} - \boldsymbol{b})^T P(M\boldsymbol{\mu} - \boldsymbol{b}) + \lambda R(\boldsymbol{\mu})\right], s.t.: \mu(i) \geq 0. \tag{3.1}$$

In Eq. (3.1), the reconstruction of the unknown vectorized CT image $\boldsymbol{\mu}$ from the measured vectorized projection $\boldsymbol{b}$, is formulated as a constrained minimization problem of an objective function $f(\boldsymbol{\mu})$ consisting of a data fidelity term and a regularization term. M is the system matrix modeling the forward projection process, P is a diagonal matrix whose diagonal elements are determined by the estimated noise variance on the projection data,[19] and $(\cdot)^T$ denotes the transpose operation. $(M\boldsymbol{\mu} - \boldsymbol{b})^T P(M\boldsymbol{\mu} - \boldsymbol{b})$ calculates the L-2 norm of the difference between the estimated and raw projections, i.e. the data fidelity error. $R(\boldsymbol{\mu})$ is a convex regularization term penalizing the roughness of the estimated image. As implemented in the existing literature,[22, 29, 79] λ is an empirically selected weighting factor which balances the strength of noise suppression and the residual data fidelity error to yield

a CT image with a satisfactory quality. Each element of $\boldsymbol{\mu}$, $\mu(i)$, is forced to be non-negative. The non-negativity constraint takes effect only in the area where the true CT image has values equal or close to zero, and it is infrequently active in the support of scanned object.[98, 103] Therefore the non-negativity constraint is omitted in the following derivation.

Without the non-negativity constraint, the minimization of $f(\boldsymbol{\mu})$ is equivalent to finding an optimal solution, $\widehat{\boldsymbol{\mu}}$, of which the objective function has a gradient of zero, i.e., $\widehat{\boldsymbol{\mu}}$ should satisfy the following condition:

$$\nabla f(\widehat{\boldsymbol{\mu}}) = M^T P(M\widehat{\boldsymbol{\mu}} - \boldsymbol{b}) + \lambda \nabla R(\widehat{\boldsymbol{\mu}}) = 0. \tag{3.2}$$

Eq. (3.2) describes the relationship between the noisy projection data $\boldsymbol{b}$ and the iteratively reconstructed CT image $\widehat{\boldsymbol{\mu}}$, and therefore the noise propagation during the reconstruction process. To find the noise of $\widehat{\boldsymbol{\mu}}$, the noise-free reconstructed image $\boldsymbol{\mu_0}$ is considered, which also satisfies Eq. (3.2)

$$M^T P(M\boldsymbol{\mu_0} - \boldsymbol{b_0}) + \lambda \nabla R(\boldsymbol{\mu_0}) = 0, \tag{3.3}$$

where $\boldsymbol{b_0}$ is the noise-free projection data. Denote $\boldsymbol{n_\mu}$ and $\boldsymbol{n_b}$ as the noise on the CT image and the projection data, respectively, i.e., $\widehat{\boldsymbol{\mu}} = \boldsymbol{\mu_0} + \boldsymbol{n_\mu}$ and $\boldsymbol{b} = \boldsymbol{b_0} + \boldsymbol{n_b}$. One obtains from Eqs. (3.2)and (3.3):

$$M^T P\big(M\boldsymbol{n_\mu} - \boldsymbol{n_b}\big) + \lambda\big(\nabla R(\widehat{\boldsymbol{\mu}}) - \nabla R(\boldsymbol{\mu_0})\big) = 0. \tag{3.4}$$

With the assumption of small $\boldsymbol{n_\mu}$, the second term of Eq. (3.4) can be simplified using Taylor expansion on ∇R at $\widehat{\boldsymbol{\mu}}$, i.e., $\nabla R(\widehat{\boldsymbol{\mu}}) - \nabla R(\boldsymbol{\mu_0}) \approx \nabla^2 R(\widehat{\boldsymbol{\mu}})\boldsymbol{n_\mu}$:

$$M^T P M \boldsymbol{n_\mu} - M^T P \boldsymbol{n_b} + \lambda \nabla^2 R(\widehat{\boldsymbol{\mu}})\boldsymbol{n_\mu} \approx 0$$
$$\Rightarrow \boldsymbol{n_\mu} \approx \left(M^T P M + \lambda \nabla^2 R(\widehat{\boldsymbol{\mu}})\right)^{-1} M^T P \boldsymbol{n_b}. \tag{3.5}$$

Note that the same derivation of image noise in regularized least square problems has been previously discussed by Fessler.[98] Based on Eq. (3.5), one can obtain noise properties of $\widehat{\boldsymbol{\mu}}$ if the noise statistics are known on the projection data. For example, the noise covariance matrix of $\widehat{\boldsymbol{\mu}}$ can be calculated from the noise covariance matrix of $\boldsymbol{b}$, Σ_b, as[98]:

$$\Sigma_\mu = E\left(\boldsymbol{n_\mu} \boldsymbol{n_\mu}^T\right) = \left(M^T P M + \lambda \nabla^2 R(\widehat{\boldsymbol{\mu}})\right)^{-1} M^T P \Sigma_b P M \left(M^T P M + \lambda \nabla^2 R(\widehat{\boldsymbol{\mu}})\right)^{-1}. \tag{3.6}$$

3.2.2 Simulation of noise propagation for iterative CT reconstruction

Unfortunately, neither Eq. (3.5) or (3.6) has practical value in studies of noise properties of general iterative CT reconstruction due to their high computational complexity. For a non-quadratic regularization term R, which is commonly used in existing iterative reconstruction algorithms,[22, 104, 105] the Hessian matrix $\nabla^2 R(\boldsymbol{\mu})$ is shift-variant and has a huge size of 10^9~10^{10} elements for the imaging geometry of current CT scanners. The storage of the Hessian matrix consumes at least 250 GB memory. It is almost impossible to calculate matrix inversion of these matrices on a standard computer.

To develop a practical algorithm of computing noise statistics on an iteratively reconstructed CT image, the following iterative reconstruction problem is considered:

$$\tilde{\boldsymbol{\mu}} = \arg\min f(\boldsymbol{\mu}) = \arg\min_{\boldsymbol{\mu}} \left[\frac{1}{2}\left(M\boldsymbol{\mu} - \tilde{\boldsymbol{b}}\right)^T P\left(M\boldsymbol{\mu} - \tilde{\boldsymbol{b}}\right) + \lambda R(\boldsymbol{\mu})\right], s.t.: \mu(i) \geq 0. \tag{3.7}$$

Eq. (3.7) is the same as Eq. (3.1) except that a different set of projections, $\tilde{\boldsymbol{b}}$, is used, which is obtained by adding simulated noise with known statistics, $\tilde{\boldsymbol{n}}_{\boldsymbol{b}}$, on the measured projection, $\boldsymbol{b}$, i.e., $\tilde{\boldsymbol{b}} = \boldsymbol{b} + \tilde{\boldsymbol{n}}_{\boldsymbol{b}}$. The solution to Eq. (3.7), $\tilde{\boldsymbol{\mu}}$, is different from that to Eq. (3.1), i.e., $\tilde{\boldsymbol{\mu}} = \hat{\boldsymbol{\mu}} + \tilde{\boldsymbol{n}}_{\boldsymbol{\mu}}$, where $\tilde{\boldsymbol{n}}_{\boldsymbol{\mu}}$ denotes the image difference caused by $\tilde{\boldsymbol{n}}_{\boldsymbol{b}}$. Ignoring the non-negativity constraint as in the previous section, one can have the following equation:

$$M^T P\left(M\tilde{\boldsymbol{\mu}} - \tilde{\boldsymbol{b}}\right) + \lambda \nabla R(\tilde{\boldsymbol{\mu}}) = 0. \tag{3.8}$$

One obtains from Eqs. (3.2) and (3.8):

$$M^T P\left(M\tilde{\boldsymbol{n}}_{\boldsymbol{\mu}} - \tilde{\boldsymbol{n}}_{\boldsymbol{b}}\right) + \lambda\left(\nabla R(\tilde{\boldsymbol{\mu}}) - \nabla R(\hat{\boldsymbol{\mu}})\right) = 0. \tag{3.9}$$

If one uses small simulated noise $\tilde{\boldsymbol{n}}_{\boldsymbol{b}}$, $\tilde{\boldsymbol{n}}_{\boldsymbol{\mu}}$ is small on the CT image. The second term of Eq. (3.9) is then simplified using Taylor expansion on ∇R at $\hat{\boldsymbol{\mu}}$, i.e., $\nabla R(\tilde{\boldsymbol{\mu}}) - \nabla R(\hat{\boldsymbol{\mu}}) \approx \nabla^2 R(\hat{\boldsymbol{\mu}})\tilde{\boldsymbol{n}}_{\boldsymbol{\mu}}$. The following equation is finally derived from Eq. (3.9):

$$\tilde{\boldsymbol{n}}_{\boldsymbol{\mu}} \approx \left(M^T P M + \lambda \nabla^2 R(\hat{\boldsymbol{\mu}})\right)^{-1} M^T P \tilde{\boldsymbol{n}}_{\boldsymbol{b}}. \tag{3.10}$$

Comparing Eqs. (3.5) and (3.10), one can conclude that the iterative reconstruction process using either Eq. (3.1) or Eq. (3.7) has the very similar noise propagation. As such, one can simulate random samples of iteratively reconstructed CT images, $\tilde{\boldsymbol{\mu}}$, by solving Eq. (3.7) using different simulated projection noise, $\tilde{\boldsymbol{n}}_{\boldsymbol{b}}$, added on the original measured projection data $\boldsymbol{b}$ of a single scan. Noise statistical analysis on these random samples of CT images ($\tilde{\boldsymbol{\mu}}$) (i.e., STD and NPS calculations) provides the noise statistical properties of the original CT image ($\hat{\boldsymbol{\mu}}$) from a single scan, as long as the simulated projection noise ($\tilde{\boldsymbol{n}}_{\boldsymbol{b}}$) obeys the same noise statistics as that of the measured projections ($\boldsymbol{n}_{\boldsymbol{b}}$).

3.2.3 A practical algorithm of computing noise statistics on an iteratively reconstructed CT image

Based on the previous finding, a practical algorithm is developed to compute the noise STD map and the NPS map on an iteratively reconstructed CT image from a single scan.

First, the CT image $\hat{\boldsymbol{\mu}}$ is reconstructed from the measured projection data $\boldsymbol{b}$ based on Eq. (3.1) using an existing iterative reconstruction algorithm.[19, 101] Generated from an estimated noise statistical model of projection data, the simulated projection noise, $\tilde{\boldsymbol{n}}_{\boldsymbol{b}}^{(i)}$, where the superscript i is an simulation index, is then added on the measured projection data ($\boldsymbol{b}$). The iterative CT reconstruction continues to generate a different CT image $\tilde{\boldsymbol{\mu}}^{(i)} = \hat{\boldsymbol{\mu}} + \tilde{\boldsymbol{n}}_{\boldsymbol{\mu}}^{(i)}$ from $\tilde{\boldsymbol{b}}^{(i)} = \boldsymbol{b} + \tilde{\boldsymbol{n}}_{\boldsymbol{b}}^{(i)}$ based on Eq. (3.7). The above process is repeated on the same measured projection added by different simulated projection noise, $\tilde{\boldsymbol{n}}_{\boldsymbol{b}}^{(i)}$, until a sufficient number N of different reconstruction images ($\tilde{\boldsymbol{\mu}}^{(i)} = \hat{\boldsymbol{\mu}} + \tilde{\boldsymbol{n}}_{\boldsymbol{\mu}}^{(i)}, i = 1,2, \dots N$) are

generated. Thus, the noise propagated from the simulated projection noise to each of the reconstructed images is:

$$\tilde{\boldsymbol{n}}_{\boldsymbol{\mu}}^{(\boldsymbol{i})} = \tilde{\boldsymbol{\mu}}^{(\boldsymbol{i})} - \hat{\boldsymbol{\mu}}. \tag{3.11}$$

Note that although $\tilde{\boldsymbol{b}}^{(\boldsymbol{i})}$ contains both the measured projection noise $\boldsymbol{n_b}$ and the simulated projection noise $\tilde{\boldsymbol{n}}_{\boldsymbol{b}}^{(\boldsymbol{i})}$, i.e. $\tilde{\boldsymbol{b}}^{(\boldsymbol{i})} = \boldsymbol{b_0} + \boldsymbol{n_b} + \tilde{\boldsymbol{n}}_{\boldsymbol{b}}^{(\boldsymbol{i})}$, the fluctuation of $\tilde{\boldsymbol{b}}^{(\boldsymbol{i})}$ from its mean in each set of simulation is the simulated projection noise $\tilde{\boldsymbol{n}}_{\boldsymbol{b}}^{(\boldsymbol{i})}$, instead of $\boldsymbol{n_b} + \tilde{\boldsymbol{n}}_{\boldsymbol{b}}^{(\boldsymbol{i})}$. This is because the measured noise $\boldsymbol{n_b}$ remains unchanged in all the simulations. Thus, in Eq. (3.11), the image noise $\tilde{\boldsymbol{n}}_{\boldsymbol{\mu}}^{(\boldsymbol{i})}$, i.e. the deviation of $\tilde{\boldsymbol{\mu}}^{(\boldsymbol{i})}$ from its mean $\hat{\boldsymbol{\mu}}$, is caused only by the fluctuation of $\tilde{\boldsymbol{b}}^{(\boldsymbol{i})}$, i.e. $\tilde{\boldsymbol{n}}_{\boldsymbol{b}}^{(\boldsymbol{i})}$. The noise statistics of each pixel in the original CT image can be estimated from the statistical analysis of the N sets of $\tilde{\boldsymbol{n}}_{\boldsymbol{\mu}}^{(\boldsymbol{i})}$.

The number of noise simulations, N, is empirically selected to balance the computation time and precision. A large N leads to a noise STD map with less uncertainty, while a small N is desired to save computation. $N = 32$ in the presented implementation, which achieves a root-mean-square error (RMSE) of less than 3 HU on the calculated noise STD map with a computation time of around 8 minutes.

3.2.3.1 Simulation of projection noise

The projection noise added on the measured projection data is simulated by a stochastic noise model describing the actual noise statistical distribution of raw projection data. Stochastic noise models of X-ray projection have been widely studied.[106] Among many factors contributing to the noise in data acquisition, the Poisson quantum noise of

detected photons plays a dominant role when imaging dose is not low. In this study, the noise is simulated on the measured photon numbers solely from the Poisson noise. The raw projections before the log operation are first converted from detector unit to photon number.[22] Noise is then simulated for each detector pixel by a Poisson random generator with a mean value of the measured photon number. The log operation is finally performed on the noisy projections to generate noisy line integrals, $\widetilde{\boldsymbol{b}}^{(i)}$.

3.2.3.2 Noise STD and NPS calculation

The image noise obtained by Eq. (3.11) is first converted from a vector form to an image form, $\tilde{n}_{\mu}^{(i)}(x,y)$, where (x,y) is the 2D pixel index. The noise STD map on the iteratively reconstructed image ($\widehat{\boldsymbol{\mu}}$) is calculated as:

$$STD(x,y) = \sqrt{\frac{1}{N}\sum_{i=1}^{N}\left(\tilde{n}_{\mu}^{(i)}(x,y)\right)^2}. \tag{3.12}$$

The NPS map is estimated as the expectation value ($\boldsymbol{E}(\cdot)$) of the square modulus of the 2D discrete Fourier transformation (DFT) on the noise[107]:

$$NPS(\omega_x,\omega_y) = \boldsymbol{E}\left(\left|DFT\left(\tilde{n}_{\mu}(x,y)\right)\right|^2\right) = \frac{1}{N}\sum_{i=1}^{N}\left|DFT\left(\tilde{n}_{\mu}^{(i)}(x,y)\right)\right|^2, \tag{3.13}$$

where (ω_x,ω_y) is the 2D index in the frequency domain. Since a finite number (N) of sets of noise are available, the expectation value is approximated by averaging the N sets of square modulus of 2D DFT on noise. In all the comparisons, the NPS map is normalized by its integrated area inside Nyquist frequency. To characterize the noise texture without

the presence of anatomical structures, the NPS map is calcualted in a ROI of uniform substance.

3.3 Evaluation

The new method is evaluated through studies on an anthropomorphic head phantom experiment and a head and neck patient. The phantom study is performed on a tabletop cone-beam CT (CBCT) system operated at 120 kVp with a full scan of 655 views. The phantom is scanned with a pulse width of 4 ms at 6 different tube current levels, 40 mA, 35 mA, 30 mA, 25 mA, 20 mA and 8 mA, to investigate the performance of the proposed method at different noise levels. The geometry of this system exactly matches that of a Varian On-Board Imager (OBI) CBCT system on the Trilogy radiation therapy machine. More details of the tabletop CBCT system can be found in Reference.[82]. The clinical patient data are acquired by Varian OBI CBCT system on a Trilogy radiation therapy machine operated at 100 kVp with a full scan of 498 views. For both studies, the projection data of each view contain 1024×768 pixels with a detector pixel size of 0.388×0.388 mm^2. The CT image is reconstructed at the central slice of the image volume, which has a dimension of 256×256 with a pixel size of 1×1 mm^2. The CT images are converted to CT number in Hounsfield Unit (HU).

The accuracy of this new method is evaluated on the anthropomorphic head phantom at each tube current levels. The phantom is repeatedly scanned and iteratively reconstructed by 48 times without changing the scan setting. The noise of each CT image is measured by subtracting the mean of the 48 CT images. The ground truths of the noise STD map and the NPS map are first calculated by Eq. (3.12) and Eq. (3.13), except that

the estimated noise $\tilde{n}_{\mu}^{(i)}(x,y)$ in Eq. (3.12) and Eq. (3.13) is replaced by the measured noise of CT images from the repeated scans. Only one set of the acquired sinograms is processed by the new method for the pixel-wise noise statistics estimation. The estimation accuracy of the noise STD map is quantified by the RMSE, i.e. the root-mean-square value of the difference between the estimated and the ground-truth noise STD maps.

In the study of NPS map estimation, the result of the new method is compared with that of the conventional method, which is described as: [108, 109]

$$NPS(\omega_x, \omega_y) = \left|DFT\left(\hat{\mu}_{ROI}(x,y) - \hat{\mu}_p(x,y)\right)\right|^2. \tag{3.14}$$

In Eq. (3.14), $\hat{\mu}_{ROI}$ denotes a uniform ROI, and $\hat{\mu}_p$is an estimated non-uniformity of $\hat{\mu}_{ROI}$ obtained by a low-order 2D polynomial fitting on $\hat{\mu}_{ROI}$.[109] The conventional method requires that the ROI is uniform such that the image in the ROI offset by its mean value is assumed to be the image noise of that ROI. However, such a uniformity requirement may not be satisfied due to the presence of the structured noise caused by artifacts.[110] Thus, the polynomial fitting is applied on the ROI to correct for the non-uniformity. Note that, when the order of the fitting polynomial is zero, $\hat{\mu}_p(x,y)$ reduces to the mean pixel value of the ROI. In this study, a third-order polynomial fitting is used to correct for the non-uniformity.

For both the new method and the conventional method, the ROI for the NPS map estimation is an area of 64×64 pixels, and the estimated NPS maps are interpolated to be 256×256 pixels. The accuracy of the NPS map estimation is quantified by the RMSE of the estimated NPS map compared with the ground truth.

To demonstrate the clinical utility, the proposed method is then implemented on a set of head and neck patient CT data. This work focus on comparing the noise statistics estimation results on the CT images reconstructed from the same dataset but by different iterative reconstruction algorithms.

Two iterative reconstruction methods are implemented as examples to evaluate the new method: the penalized weighted least-square (PWLS) algorithm[19] and the total variation (TV) regularization[101]. Both the PWLS method and the TV method have the same framework of regularization-based optimization as shown in Eq. (3.1). The regularization term ($R(\boldsymbol{\mu})$ in Eq. (3.1)) of PWLS is

$$R(\boldsymbol{\mu}) = \frac{1}{2}\sum_j \sum_{m\in N_j} a_{jm}\left(\mu_j - \mu_m\right)^2, \tag{3.15}$$

where index j runs over all image pixels, and N_j represents the set of eight neighbors of the j-th image pixel in two dimensions. The weight a_{jm} is equal to 1 for the vertical and horizontal neighbors and $1/\sqrt{2}$ for the diagonal neighbors. The regularization term of TV is $R(\boldsymbol{\mu}) = \|\boldsymbol{\mu}\|_{TV}$, where $\|\cdot\|_{TV}$ is the TV term defined as the L1 norm of the spatial gradient image.[22] In Eq. (3.1), the difference between the measured projection and the forwarded projection of reconstructed image is weighted by W in order to achieve noise uniformity across the image. W is a diagonal matrix with the i-th element of the reciprocal of the estimated noise variance on the projection data at the i-th detector bin. In the head phantom study, to demonstrate the performance of the proposed method on estimating both heterogeneous and homogeneous noise STD maps, both uniform and variant weights W are used in investigations. The gradient projection method described in Reference[22] is used

as the iterative update scheme for both methods. In all comparisons, the weighting factors of the regularization terms in PWLS and TV are tuned to achieve the same data fidelity value on the reconstructed images obtained by the two algorithms.

The iterative CT reconstruction methods as well as the new algorithm of noise STD and NPS calculation are implemented in Matlab on a 1.8 GHz computer with 16GB internal memory and a NVIDIA® Quadro K4000 GPU. For each case, it takes about 15 seconds to obtain an iteratively reconstructed CT image, and 8 minutes to generate noise STD and NPS maps.

3.4 Results

3.4.1 Head phantom study

The accuracy of the new method is evaluated on the anthropomorphic head phantom. Figure 3.1 shows the iteratively reconstructed CT images of the head phantom, the noise STD maps of the ground truths and the estimated results by the new method. Note that the results at flux levels of 8 mA and 40 mA are taken as examples and shown in Figure 3.1 since it is found that the results ranging from 20 mA to 40 mA are quite similar. It is seen that the estimated noise STD maps of images reconstructed by PWLS and TV (column (2)) at both flux levels (8 mA and 40 mA) match their corresponding ground truths (column (3)) very well. The difference between the estimation and the ground truth is shown in the fourth column with a narrow display window. Table 3-I shows the RMSEs of the estimated noise STD maps compared with the ground truths at all flux levels. The accuracies of estimated noise STD maps are similar at different flux levels ranging from 20 mA to 40 mA, and it slightly degrades at 8 mA. Overall, the proposed algorithm performs well in all

different scenarios, with a RMSE less than 5 HU. The new method clearly reveals the difference between the noise STD maps of CT images of PWLS and TV. On the PWLS results, the noise STDs (Figure 3.1 (a3), (b3), (e3) and (f3)) are uniform in the support of scanned object, while for TV, the noise STDs (Figure 3.1 (c3), (d3), (g3), (h3)) of pixels around sharp transitions are significantly higher than those in the uniform area. The above finding is consistent with the existing literature.[111, 112]

Figure 3.2 shows the NPS maps of the ground truth and the estimated results by the conventional method and the new method at flux levels of 8 mA and 40 mA. On both PWLS and TV reconstructions, the estimations (column (2)) match with the ground truths (column (1)) overall, while the results of the conventional method (column (3)) appear noisy and inaccurate. The accuracies of the estimated NPS map at all flux levels are summarized in Table 3-I. Compared with the conventional method, the new method achieves 92% less RMSE on average. The new method also reveals the difference between the NPS maps on CT images reconstructed by PWLS (Figure 3.2 (a2), (b2), (e2) and (f2)) and TV (Figure 3.2 (c2), (d2), (g2) and (h2)). The image reconstructed by TV contains more low-frequency noise than that by PWLS.

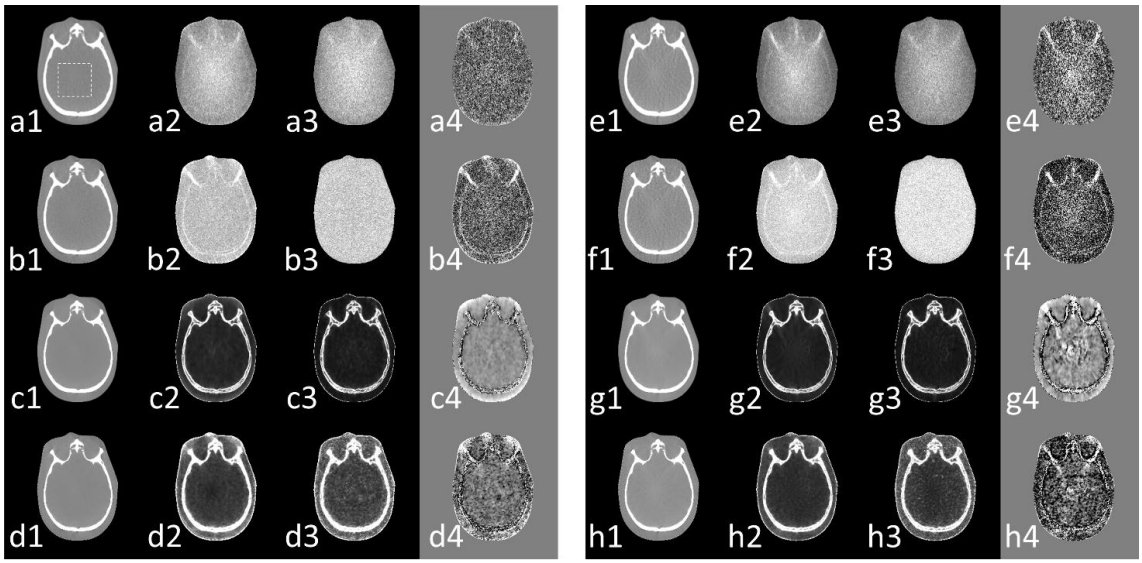

Figure 3.1 CT images and noise STD maps of the anthropomorphic head phantom using (a) PWLS with uniform W (i.e., W in Eq. (1)) at 40 mA, (b) PWLS with variant W at 40 mA, (c) TV with uniform W at 40 mA, (d) TV with variant W at 40 mA, (e) PWLS with uniform W at 8 mA, (f) PWLS with variant W at 8 mA, (g) TV with uniform W at 8 mA, (h) TV with variant W at 8 mA. Columns: (1) the reconstructed CT images using iterative methods; (2) the ground truth of noise STD maps; (3) the estimated noise STD maps; (4) the smoothed difference maps between the estimated and ground truth of noise STD maps. The dash square in (a1) indicates the ROI where the NPS maps shown in Figure 3.2 are calculated. Display windows: [-500 500] HU for column (1), [0 20] HU for column (2) and (3) from (a) to (d), [0 40] HU for column (2) and (3) from (e) to (h), and [-5 5] HU for column (4).

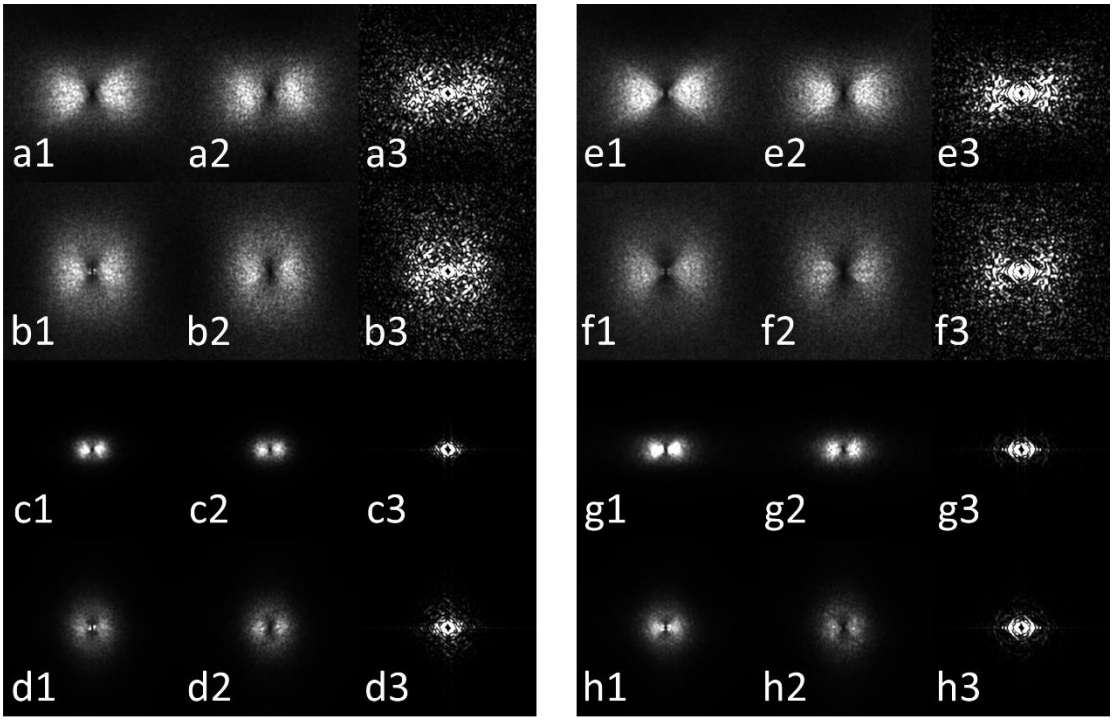

Figure 3.2 NPS maps of the CT images of the anthropomorphic head phantom using (a) PWLS with uniform W (i.e., W in Eq. (1)) at 40 mA, (b) PWLS with variant W at 40 mA, (c) TV with uniform W at 40 mA, (d) TV with variant W at 40 mA, (e) PWLS with uniform W at 8 mA, (f) PWLS with variant W at 8 mA, (g) TV with uniform W at 8 mA, (h) TV with variant W at 8 mA. Columns (1), (2) and (3) show the NPS maps of the ground truth, estimated by the proposed method and estimated by the conventional method, respectively. The ROI where the NPS maps are calculated is indicated as the dash square in Figure 3.1(a1). Display window: [0 1]$\times 10^{-4}$ for (a), (b), (e) and (f), and [0 5] $\times 10^{-4}$ for (c), (d), (g) and (h).

Table 3-I RMSE of the estimated noise STD maps and NPS maps.

		Noise STD maps by proposed method (HU)		NPS maps ($\times 10^{-6}$)			
Weight W	Flux level	PWLS	TV	Proposed method		Conventional method	
				PWLS	TV	PWLS	TV
Uniform	40	1.51	1.85	5.47	17.90	46.09	217.92
	35	1.88	2.38	5.83	19.65	41.93	200.87
	30	1.54	1.97	6.11	18.54	51.12	203.42
	25	1.84	2.26	5.58	19.07	48.23	202.21
	20	1.80	2.51	5.94	22.34	67.61	173.82
	8	2.62	3.31	5.81	20.82	80.06	183.35
Variant	40	2.98	2.83	4.88	20.43	51.88	180.48
	35	3.22	3.26	5.29	22.49	45.57	160.19
	30	2.69	2.96	6.19	31.92	40.89	186.96
	25	2.91	3.20	5.77	22.61	56.67	198.14
	20	3.27	3.36	4.92	28.66	52.70	176.50
	8	4.53	4.55	5.09	20.15	58.49	175.56

3.4.2 Head and neck patient study

The clinical utility of the new method is then demonstrated by the implementation on a head and neck patient. The noise STD maps and the NPS maps estimated by the new method along with the reconstructed images of PWLS and TV are shown in Figure 3.3. The new method provides a detailed evaluation of imaging performances of different

iterative reconstruction algorithms on the same CT dataset. For example, the comparison between the noise STD maps (Figure 3.3(a2) and 4(b2)) indicates that although the CT images reconstructed by PWLS and TV appear similar, the reconstruction uncertainty (i.e., the noise STD) significantly varies across the image. The reconstruction uncertainty of PWLS is more uniform, while the TV method tends to have large noise around sharp edges. The above difference is also clearly seen in the 1D profile comparison of the noise STD shown in Figure 3.4. The comparison on the NPS maps (Figure 3.3(a3) and 4(b3)) demonstrates that the noise texture of the image reconstructed by TV is coarser (i.e., predominantly low-frequency) than that by PWLS in this clinical case.[113, 114]

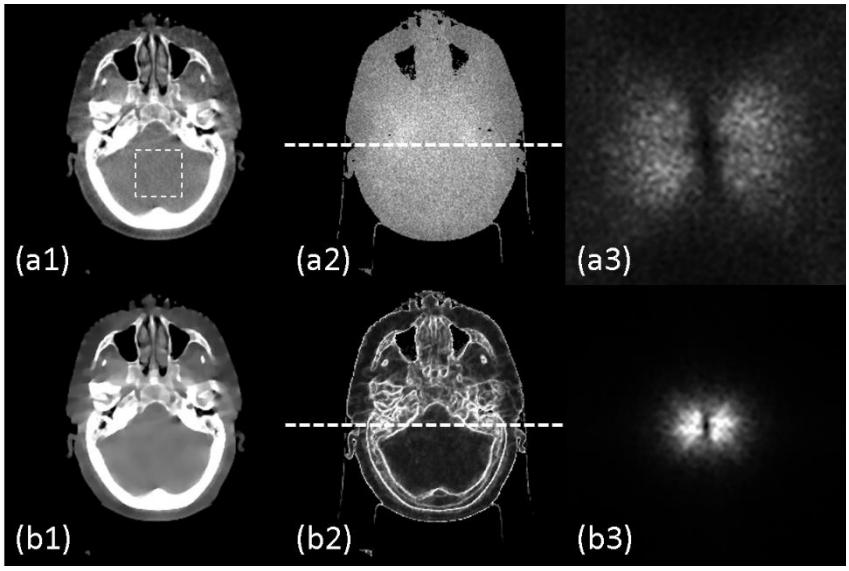

Figure 3.3 CT images, noise STD maps and NPS maps. Column (1) shows the reconstructed CT images using iterative methods. Columns (2) and (3) are the noise STD maps and NPS maps estimated by the new method, respectively. The iterative methods used in rows (a) and (b) are PWLS and TV, respectively. The dash square in (a1) indicates the ROI where the NPS map is calculated. The dashed lines in (a2) and (b2) indicate where the noise STD profiles shown in Figure 3.4 are plotted. Display window: [-500 500] HU for (a1) and (b1), [0 80] HU for (a2) and (b2), [0 1]$\times 10^{-4}$ for (a3) and [0 4]$\times 10^{-4}$ for (b3) .

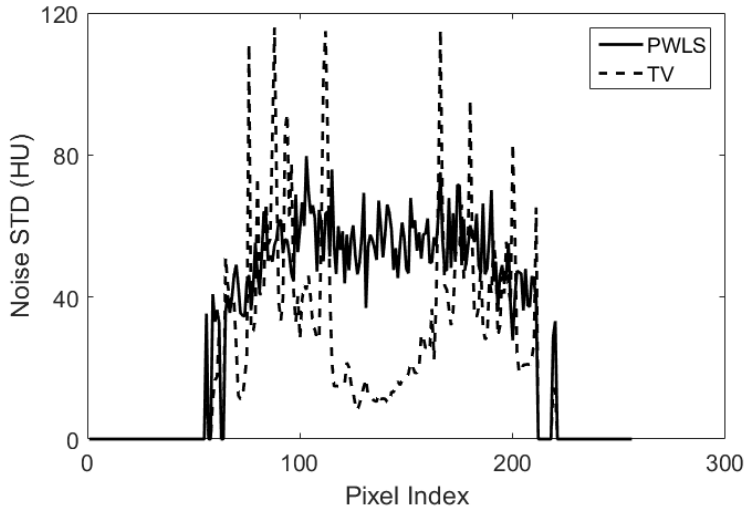

Figure 3.4 Noise STD profiles of the CT images reconstructed by PWLS and TV. The dashed lines in Figure 3.3 (a2) and (b2) are where the profiles are plotted.

3.5 Conclusions and discussion

In this study, a practical method is developed for pixel-wise estimation of noise statistics for an iteratively reconstructed CT image from a single scan, which enables an accurate calculation of noise STD and NPS maps. On an anthropomorphic head phantom, it is demonstrated that the new method accurately estimates the noise STD map with an RMSE of less than 5HU, and substantially improves over the conventional NPS estimation method by decreasing the RMSE of NPS maps by 92%. The implementation of the new method on clinical data successfully provides the noise STD values around complex structures and a high-quality NPS map. Moreover, the new algorithm provides a detailed evaluation of noise properties of different iterative reconstruction methods on the same CT dataset.

In the new method, additional noise is simulated on the measured noisy data from a single scan. Although noise realizations are commonly used in simulation to study image

statistics, the new method is distinct. Most of the existing studies start from a noiseless ground truth, which is unavailable for a clinical dataset, and simulate additional noise on projection data to investigate the resultant CT image noise. In this study, via mathematical derivations, it shows that simulation of additional noise on one single set of noisy data leads to the same noise propagation in the iterative CT reconstruction process and therefore one can accurately estimate noise of a CT image using multiple noise realizations. The novelty of this work lies in that multiple CT scans are successfully replaced by multiple noise realizations toward the purpose of CT noise estimation, which makes this algorithm practically useful on clinical data.

The success of this new method in estimating the noise STD and NPS maps stems from the accurate noise propagation model. In this method, pixel-wise noise statistics are estimated from multiple sets of image noise, each of which contains exclusively the stochastic fluctuation at each pixel caused by the simulated projection noise through the reconstruction process. Whereas in the conventional method, the noise estimated in ROI may still contain residual structured noise that cannot be completely corrected by the polynomial fitting and therefore downgrades the accuracy of noise STD or NPS estimation.

The non-negativity constraint in Eq. (3.1) is ignored in the new method to simplify the algorithm derivation. As the non-negativity constraint takes effect only in the image area with CT values close to air (according to the KKT condition in the optimization theory), ignoring the non-negativity constraint would affect the accuracy of noise estimation only outside the patient body or in air cavities (e.g., lungs or gas pockets), which has limited impact on the clinical use of the new algorithm.

The N samples of CT image noise $\tilde{\boldsymbol{n}}_{\boldsymbol{\mu}}^{(\boldsymbol{i})}$ obtained by the new algorithm allows calculations of different noise properties, not limited to the noise STD and NPS maps as shown in this paper. For example, it is possible to estimate the noise autocorrelation $R(x_1, y_1; x_2, y_2) = \sum_{i=1}^{N} \tilde{n}_{\mu}^{(i)}(x_1, y_1)\tilde{n}_{\mu}^{(i)}(x_2, y_2)$ between any two pixels at (x_1, y_1) and (x_2, y_2) on an iteratively reconstructed CT images with a higher accuracy than the conventional method. The current estimation of noise autocorrelation on a single CT image can be applied on only uniform ROIs,[115] while the new method calculates the noise autocorrelation between any two pixels.

The clinical utility of this new method are shown on data of a head and neck patient, using PWLS and TV as examples of iterative reconstruction algorithms. This algorithm is generic as long as the iterative reconstruction has a form of Eq. (3.1). Using similar derivations of noise perturbation, one can extend the algorithm to other iterative CT reconstruction that is formulated as a convex optimization problem. The obtained noise properties are useful in the evaluations of iterative reconstruction algorithms toward different clinical tasks. For example, the comparison between the noise STD and NPS maps of the images reconstructed by TV and PWLS (Figure 3.3(a2) and (b2), Figure 3.4) shows that the two algorithms have different imaging advantages across the field in the presented head and neck patient case. The TV reconstruction achieves lower uncertainties in the uniform area than the PWLS reconstruction. However, the NPS comparison indicates significant high-frequency loss on the image reconstructed by the TV algorithm.

CHAPTER 4. SUMMARY AND FUTURE DIRECTIONS

In this dissertation, novel methods have been developed for image reconstruction and noise estimation in CT imaging. A new iterative reconstruction method, SPIR, for DECT is introduced in Chapter 2. This method enables a new data acquisition scheme which requires one full scan and a second sparse-view scan for potential reduction in imaging dose and engineering cost of DECT. The redundant structural information from the full scan is extracted and used to aid the reconstruction of the sparse view scan. The performance of the proposed method is evaluated on both digital and physical phantoms.

In Chapter 3, a practical method for pixel-wise calculation of noise statistics on an iteratively reconstructed CT image is introduced to enable accurate evaluation of noise standard deviation (STD) for each pixel and noise power spectrum. It shows that the model of noise propagation of iterative reconstruction remains approximately unchanged for extra simulated noise added to the measured projections. Thus, the noise performance of iteratively reconstructed image can be evaluated by the noise analysis on multiple images iteratively reconstructed from same measured dataset with different noise simulated from an estimated projection noise model. The method is evaluated on an anthropomorphic head phantom, and demonstrate its clinical utility on a set of head and neck patient CT data.

The new SPIR algorithm described in Chapter 2 can be further assessed and improved. For example, the method of generating similarity matrix W described in this dissertation is not the only solution of structure classification for SPIR. It is suggested that more sophisticated image segmentation methods for improved calculation of the similarity matrix.

In the result part of Chapter 3, it is found that the accuracies of the estimated noise STD maps are similar at flux levels ranging from 20 mA to 40 mA, but show slightly larger errors at the lowest flux level (8 mA) in Table 3-I. A major source of the error could be that the noise on the measured photon numbers is simulated solely from the Poisson noise and neglect the electronic noise which may play an important role at low flux.[116] The method performance can be further improved by incorporating a more sophisticated noise model which considers other factors contributing to the noise in the CT data acquisition.

REFERENCES

[1] G.N. Hounsfield, "Computerized transverse axial scanning (tomography). 1. Description of system," Br J Radiol **46**, 1016-1022 (1973).

[2] OECD, *Health at a glance 2015*. (OECD Publishing).

[3] J. Xu, M. Mahesh, B.M.W. Tsui, "Is iterative reconstruction ready for MDCT?," Journal of the American College of Radiology : JACR **6**, 274-276 (2009).

[4] M.K. Kalra, M.M. Maher, T.L. Toth, L.M. Hamberg, M.A. Blake, J.-A. Shepard, S. Saini, "Strategies for CT radiation dose optimization," Radiology **230**, 619-628 (2004).

[5] E.C. Lin, "Radiation risk from medical imaging," Mayo Clinic Proceedings **85**, 1142-1146 (2010).

[6] P.K. Nguyen, J.C. Wu, "Radiation exposure from imaging tests: is there an increased cancer risk?," Expert Review of Cardiovascular Therapy **9**, 177-183 (2011).

[7] D.J. Brenner, E.J. Hall, "Computed tomography--an increasing source of radiation exposure," New England Journal of Medicine **357**, 2277-2284 (2007).

[8] W.A. Kalender, H. Wolf, C. Suess, "Dose reduction in CT by anatomically adapted tube current modulation. II. Phantom measurements," Medical Physics **26**, 2248-2253 (1999).

[9] L. Yu, X. Liu, S. Leng, J.M. Kofler, J.C. Ramirez-Giraldo, M. Qu, J. Christner, J.G. Fletcher, C.H. McCollough, "Radiation dose reduction in computed tomography: techniques and future perspective," Imaging In Medicine **1**, 65-84 (2009).

[10] K. Taguchi, M. Zhang, E.C. Frey, X. Wang, J.S. Iwanczyk, E. Nygard, N.E. Hartsough, B.M. Tsui, W.C. Barber, "Modeling the performance of a photon counting x-ray detector for CT: energy response and pulse pileup effects," Medical Physics **38**, 1089-1102 (2011).

[11] E. Roessl, R. Proksa, "K-edge imaging in x-ray computed tomography using multi-bin photon counting detectors," Physics in Medicine and Biology **52**, 4679-4696 (2007).

[12] W.A. Kalender, P. Deak, M. Kellermeier, M. van Straten, S.V. Vollmar, "Application- and patient size-dependent optimization of x-ray spectra for CT," Medical Physics **36**, 993-1007 (2009).

[13] L. Yu, M.R. Bruesewitz, K.B. Thomas, J.G. Fletcher, J.M. Kofler, C.H. McCollough, "Optimal tube potential for radiation dose reduction in pediatric CT: Principles, clinical implementations, and pitfalls," RadioGraphics **31**, 835-848 (2011).

[14] B. Lu, H. Lu, J. Palta, "A comprehensive study on decreasing the kilovoltage cone-beam CT dose by reducing the projection number," Journal of applied clinical medical physics / American College of Medical Physics **11**, 3274 (2010).

[15] A.K. Hara, R.G. Paden, A.C. Silva, J.L. Kujak, H.J. Lawder, W. Pavlicek, "Iterative reconstruction technique for reducing body radiation dose at CT: feasibility study," American Journal of Roentgenology **193**, 764-771 (2009).

[16] L.L. Geyer, U.J. Schoepf, F.G. Meinel, J. John W. Nance, G. Bastarrika, J.A. Leipsic, N.S. Paul, M. Rengo, A. Laghi, C.N.D. Cecco, "State of the art: Iterative CT reconstruction techniques," Radiology **276**, 339-357 (2015).

[17] R.A. Brooks, G. Di Chiro, "Principles of computer assisted tomography (CAT) in radiographic and radioisotopic imaging," Physics in Medicine and Biology **21**, 689-732 (1976).

[18] K. Li, J. Tang, G.H. Chen, "Statistical model based iterative reconstruction (MBIR) in clinical CT systems: experimental assessment of noise performance," Medical Physics **41**, 041906 (2014).

[19] J.A. Fessler, "Penalized weighted least-squares image reconstruction for positron emission tomography," IEEE Transactions on Medical Imaging **13**, 290-300 (1994).

[20] J.B. Thibault, K.D. Sauer, C.A. Bouman, J. Hsieh, "A three-dimensional statistical approach to improved image quality for multislice helical CT," Medical Physics **34**, 4526-4544 (2007).

[21] E.Y. Sidky, X. Pan, "Image reconstruction in circular cone-beam computed tomography by constrained, total-variation minimization," Physics in Medicine and Biology **53**, 4777-4807 (2008).

[22] T. Niu, L. Zhu, "Accelerated barrier optimization compressed sensing (ABOCS) reconstruction for cone-beam CT: phantom studies," Medical Physics **39**, 4588-4598 (2012).

[23] S. Singh, M.K. Kalra, M.D. Gilman, J. Hsieh, H.H. Pien, S.R. Digumarthy, J.-A.O. Shepard, "Adaptive statistical iterative reconstruction technique for radiation dose reduction in chest CT: A pilot study," Radiology **259**, 565-573 (2011).

[24] J. Fan, M. Yue, R. Melnyk, "Benefits of ASiR-V reconstruction for reducing patient radiation dose and preserving diagnostic quality in CT exams," White Paper, GE Healthcare 2014).

[25] Y. Funama, K. Taguchi, D. Utsunomiya, S. Oda, Y. Yanaga, Y. Yamashita, K. Awai, "Combination of a low tube voltage technique with the hybrid iterative reconstruction (iDose) algorithm at coronary CT angiography," Journal of Computer Assisted Tomography **35**, 480-485 (2011).

[26] P.B. Noel, A.A. Fingerle, B. Renger, D. Munzel, E.J. Rummeny, M. Dobritz, "Initial performance characterization of a clinical noise-suppressing reconstruction algorithm for MDCT," American Journal of Roentgenology **197**, 1404-1409 (2011).

[27] S. Baumueller, A. Winklehner, C. Karlo, R. Goetti, T. Flohr, E.W. Russi, T. Frauenfelder, H. Alkadhi, "Low-dose CT of the lung: potential value of iterative reconstructions," European Radiology **22**, 2597-2606 (2012).

[28] A. Padole, R.D. Ali Khawaja, M.K. Kalra, S. Singh, "CT Radiation Dose and Iterative Reconstruction Techniques," American Journal of Roentgenology **204**, W384-W392 (2015).

[29] X. Jia, B. Dong, Y. Lou, J.S. B., "GPU-based iterative cone-beam CT reconstruction using tight frame regularization," Physics in Medicine and Biology **56**, 3787 (2011).

[30] J.H. Pachon, G. Yadava, D. Pal, J. Hsieh, "Image quality evaluation of iterative CT reconstruction algorithms: a perspective from spatial domain noise texture measures," Proc. SPIE **8313**, 83132K-83132K-83139 (2012).

[31] R.E. Alvarez, A. Macovski, "Energy-selective reconstructions in X-ray computerised tomography," Physics in Medicine and Biology **21**, 733 (1976).

[32] E.Y. Sidky, Y. Zou, X. Pan, "Impact of polychromatic x-ray sources on helical, cone-beam computed tomography and dual-energy methods," Physics in Medicine and Biology **49**, 2293 (2004).

[33] X. Dong, T. Niu, L. Zhu, "Combined iterative reconstruction and image-domain decomposition for dual energy CT using total-variation regularization," Medical Physics **41**, 051909 (2014).

[34] T.P. Szczykutowicz, G.-H. Chen, "Dual energy CT using slow kVp switching acquisition and prior image constrained compressed sensing," Physics in Medicine and Biology **55**, 6411 (2010).

[35] P. Sukovic, N.H. Clinthorne, "Penalized weighted least-squares image reconstruction for dual energy X-ray transmission tomography," IEEE Transactions on Medical Imaging **19**, 1075-1081 (2000).

[36] L. Yu, S. Leng, C.H. McCollough, "Dual-energy CT-based monochromatic imaging," American Journal of Roentgenology **199**, S9-s15 (2012).

[37] P. Stenner, T. Berkus, M. Kachelriess, "Empirical dual energy calibration (EDEC) for cone-beam computed tomography," Medical Physics **34**, 3630-3641 (2007).

[38] B. Li, "Dual-energy CT with fast-kvp switching and its applications in orthopedics," OMICS Journal of Radiology **2**, - (2013).

[39] D. Xu, D.A. Langan, X. Wu, J.D. Pack, T.M. Benson, J.E. Tkaczky, A.M. Schmitz, "Dual energy CT via fast kVp switching spectrum estimation," Proc. SPIE **7258**, 72583T-72583T-72510 (2009).

[40] C.H. McCollough, S. Leng, L. Yu, J.G. Fletcher, "Dual- and multi-energy CT: Principles, technical approaches, and clinical applications," Radiology **276**, 637-653 (2015).

[41] M. Petersilka, H. Bruder, B. Krauss, K. Stierstorfer, T.G. Flohr, "Technical principles of dual source CT," European Journal of Radiology **68**, 362-368 (2008).

[42] F. Kelcz, P.M. Joseph, S.K. Hilal, "Noise considerations in dual energy CT scanning," Medical Physics **6**, 418-425 (1979).

[43] A.N. Primak, J.C. Ramirez Giraldo, X. Liu, L. Yu, C.H. McCollough, "Improved dual-energy material discrimination for dual-source CT by means of additional spectral filtration," Medical Physics **36**, 1359-1369 (2009).

[44] M. Petersilka, K. Stierstorfer, H. Bruder, T. Flohr, "Strategies for scatter correction in dual source CT," Medical Physics **37**, 5971-5992 (2010).

[45] J. Tanguay, H.K. Kim, I.A. Cunningham, "The role of x-ray Swank factor in energy-resolving photon-counting imaging," Medical Physics **37**, 6205-6211 (2010).

[46] K. Zhang, G. Rosenbaum, G. Bunker, "Energy-resolving X-ray fluorescence detection using synthetic multilayers," J Synchrotron Radiat **5**, 1227-1234 (1998).

[47] D. Murphy, S. Alaamri, "Technical advancements in dual energy," in *Dual-Energy CT in Cardiovascular Imaging*, edited by P.M. Carrascosa, R.C. Cury, M.J. García, J.A. Leipsic (Springer International Publishing, 2015), pp. 151-172.

[48] T.R.C. Johnson, "Dual-energy CT: General principles," American Journal of Roentgenology **199**, S3-S8 (2012).

[49] B. Ruzsics, H. Lee, P.L. Zwerner, M. Gebregziabher, P. Costello, U.J. Schoepf, "Dual-energy CT of the heart for diagnosing coronary artery stenosis and myocardial ischemia-initial experience," European Journal of Radiology **18**, 2414-2424 (2008).

[50] D.N. Tran, M. Straka, J.E. Roos, S. Napel, D. Fleischmann, "Dual-energy CT discrimination of iodine and calcium: experimental results and implications for lower extremity CT angiography," Academic Radiology **16**, 160-171 (2009).

[51] Y. Watanabe, K. Uotani, T. Nakazawa, M. Higashi, N. Yamada, Y. Hori, S. Kanzaki, T. Fukuda, T. Itoh, H. Naito, "Dual-energy direct bone removal CT angiography for evaluation of intracranial aneurysm or stenosis: comparison with conventional digital subtraction angiography," European Journal of Radiology **19**, 1019-1024 (2009).

[52] T. Kau, W. Eicher, C. Reiterer, M. Niedermayer, E. Rabitsch, B. Senft, K.A. Hausegger, "Dual-energy CT angiography in peripheral arterial occlusive disease-accuracy of maximum intensity projections in clinical routine and subgroup analysis," European Journal of Radiology **21**, 1677-1686 (2011).

[53] S.F. Thieme, V. Graute, K. Nikolaou, D. Maxien, M.F. Reiser, M. Hacker, T.R. Johnson, "Dual Energy CT lung perfusion imaging--correlation with SPECT/CT," European Journal of Radiology **81**, 360-365 (2012).

[54] L.J. Zhang, C.S. Zhou, U.J. Schoepf, H.X. Sheng, S.Y. Wu, A.W. Krazinski, J.R. Silverman, F.G. Meinel, Y.E. Zhao, Z.J. Zhang, G.M. Lu, "Dual-energy CT lung ventilation/perfusion imaging for diagnosing pulmonary embolism," European Journal of Radiology **23**, 2666-2675 (2013).

[55] A.N. Primak, J.G. Fletcher, T.J. Vrtiska, O.P. Dzyubak, J.C. Lieske, M.E. Jackson, J.C. Williams, Jr., C.H. McCollough, "Noninvasive differentiation of uric acid versus non-uric acid kidney stones using dual-energy CT," Academic Radiology **14**, 1441-1447 (2007).

[56] A. Graser, T.R. Johnson, H. Chandarana, M. Macari, "Dual energy CT: preliminary observations and potential clinical applications in the abdomen," European Journal of Radiology **19**, 13-23 (2009).

[57] G. Hidas, R. Eliahou, M. Duvdevani, P. Coulon, L. Lemaitre, O.N. Gofrit, D. Pode, J. Sosna, "Determination of renal stone composition with dual-energy CT: in vivo analysis and comparison with x-ray diffraction," Radiology **257**, 394-401 (2010).

[58] J. Hatton, B. McCurdy, P.B. Greer, "Cone beam computerized tomography: the effect of calibration of the Hounsfield unit number to electron density on dose calculation accuracy for adaptive radiation therapy," Physics in Medicine and Biology **54**, N329-346 (2009).

[59] M. Yang, G. Virshup, J. Clayton, X.R. Zhu, R. Mohan, L. Dong, "Theoretical variance analysis of single- and dual-energy computed tomography methods for calculating proton stopping power ratios of biological tissues," Physics in Medicine and Biology **55**, 1343 (2010).

[60] C.N. De Cecco, V. Buffa, S. Fedeli, M. Luzietti, A. Vallone, R. Ruopoli, V. Miele, M. Rengo, P. Paolantonio, M. Maurizi Enrici, A. Laghi, V. David, "Dual energy CT (DECT) of the liver: conventional versus virtual unenhanced images," European Journal of Radiology **20**, 2870-2875 (2010).

[61] V.A. Sahni, A.B. Shinagare, S.G. Silverman, "Virtual unenhanced CT images acquired from dual-energy CT urography: accuracy of attenuation values and variation with contrast material phase," Clin Radiol **68**, 264-271 (2013).

[62] R.K. Kaza, J.F. Platt, R.H. Cohan, E.M. Caoili, M.M. Al-Hawary, A. Wasnik, "Dual-energy CT with single- and dual-source scanners: Current applications in evaluating the genitourinary tract," RadioGraphics **32**, 353-369 (2012).

[63] E.Y. Sidky, Y. Zou, X. Pan, "Impact of polychromatic x-ray sources on helical, cone-beam computed tomography and dual-energy methods," Physics in Medicine and Biology **49**, 2293-2303 (2004).

[64] J. Hsieh, "TU-E-210A-01: Dual-energy CT with fast-kVp switch," Medical Physics **36**, 2749-2749 (2009).

[65] E.Y. Sidky, C.-M. Kao, X. Pan, "Accurate image reconstruction from few-views and limited-angle data in divergent-beam CT," Journal of X-Ray Science and Technology **14**, 119-139 (2006).

[66] J. Bian, J.H. Siewerdsen, X. Han, E.Y. Sidky, J.L. Prince, C.A. Pelizzari, X. Pan, "Evaluation of sparse-view reconstruction from flat-panel-detector cone-beam CT," Physics in Medicine and Biology **55**, 6575 (2010).

[67] R. Ludwig, B. Frank, F. Christof, K. Marc, "Improved total variation-based CT image reconstruction applied to clinical data," Physics in Medicine and Biology **56**, 1545 (2011).

[68] H. Kudo, T. Suzuki, E.A. Rashed, "Image reconstruction for sparse-view CT and interior CT-introduction to compressed sensing and differentiated backprojection," Quantitative Imaging in Medicine and Surgery **3**, 147-161 (2013).

[69] Y. Zhang, J. Huang, J. Ma, H. Zhang, Z. Bian, D. Zeng, Y. Gao, W. Chen, "Iterative image reconstruction for ultra-low-dose CT with a combined low-mAs and sparse-view protocol," Conference proceedings : ... Annual International Conference of the IEEE Engineering in Medicine and Biology Society. IEEE Engineering in Medicine and Biology Society. Annual Conference **2013**, 5107-5110 (2013).

[70] M. Li, H. Yang, H. Kudo, "An accurate iterative reconstruction algorithm for sparse objects: application to 3D blood vessel reconstruction from a limited number of projections," Physics in Medicine and Biology **47**, 2599 (2002).

[71] E. Hansis, D. Schafer, O. Dossel, M. Grass, "Evaluation of iterative sparse object reconstruction from few projections for 3-D rotational coronary angiography," IEEE Transactions on Medical Imaging **27**, 1548-1555 (2008).

[72] Y. Liu, Z. Liang, J. Ma, H. Lu, K. Wang, H. Zhang, W. Moore, "Total variation-stokes strategy for sparse-view X-ray CT image reconstruction," IEEE Transactions on Medical Imaging **33**, 749-763 (2014).

[73] S. Leng, J. Tang, J. Zambelli, B. Nett, R. Tolakanahalli, G.H. Chen, "High temporal resolution and streak-free four-dimensional cone-beam computed tomography," Physics in Medicine and Biology **53**, 5653-5673 (2008).

[74] H. Lee, L. Xing, R. Davidi, R. Li, J. Qian, R. Lee, "Improved compressed sensing-based cone-beam CT reconstruction using adaptive prior image constraints," Physics in Medicine and Biology **57**, 2287 (2012).

[75] S. Cho, E. Pearson, E.Y. Sidky, J. Bian, C.A. Pelizzari, X. Pan, "Prior-image-based few-view cone beam CT for applications to daily scan in image-guided radiation therapy: preliminary study," Proc. SPIE **7258**, 72581U (2009).

[76] G.H. Chen, J. Tang, J. Hsieh, "Temporal resolution improvement using PICCS in MDCT cardiac imaging," Medical Physics **36**, 2130-2135 (2009).

[77] J. Tang, J. Hsieh, G.H. Chen, "Temporal resolution improvement in cardiac CT using PICCS (TRI-PICCS): performance studies," Medical Physics **37**, 4377-4388 (2010).

[78] B. Junguo, H.S. Jeffrey, H. Xiao, Y.S. Emil, L.P. Jerry, A.P. Charles, P. Xiaochuan, "Evaluation of sparse-view reconstruction from flat-panel-detector cone-beam CT," Physics in Medicine and Biology **55**, 6575 (2010).

[79] G.H. Chen, J. Tang, S. Leng, "Prior image constrained compressed sensing (PICCS): a method to accurately reconstruct dynamic CT images from highly undersampled projection data sets," Medical Physics **35**, 660-663 (2008).

[80] C. Tomasi, R. Manduchi, "Bilateral filtering for gray and color images," Computer Vision, 1998. Sixth International Conference on, 839-846 (1998).

[81] L. Zhu, N.R. Bennett, R. Fahrig, "Scatter correction method for X-ray CT using primary modulation: theory and preliminary results," IEEE Transactions on Medical Imaging **25**, 1573-1587 (2006).

[82] T. Niu, L. Zhu, "Scatter correction for full-fan volumetric CT using a stationary beam blocker in a single full scan," Medical Physics **38**, 6027-6038 (2011).

[83] T. Niu, X. Dong, M. Petrongolo, L. Zhu, "Iterative image-domain decomposition for dual-energy CT," Medical Physics **41**, 041901 (2014).

[84] J. Song, Q.H. Liu, G.A. Johnson, C.T. Badea, "Sparseness prior based iterative image reconstruction for retrospectively gated cardiac micro-CT," Medical Physics **34**, 4476-4483 (2007).

[85] J.C. Park, B. Song, J.S. Kim, S.H. Park, H.K. Kim, Z. Liu, T.S. Suh, W.Y. Song, "Fast compressed sensing-based CBCT reconstruction using Barzilai-Borwein formulation for application to on-line IGRT," Medical Physics **39**, 1207-1217 (2012).

[86] M. Petrongolo, X. Dong, L. Zhu, "A general framework of noise suppression in material decomposition for dual-energy CT," Medical Physics **42**, 4848-4862 (2015).

[87] S. Richard, J.H. Siewerdsen, "Optimization of dual-energy imaging systems using generalized NEQ and imaging task," Medical Physics **34**, 127-139 (2007).

[88] J.M. Sabol, G.B. Avinash, F. Nicolas, B.E.H. Claus, J. Zhao, J.T. Dobbins Iii, " Development and characterization of a dual-energy subtraction imaging system for chest radiography based on CsI:Tl amorphous silicon flat-panel technology " Proc. SPIE **4320**, 399-408 (2001).

[89] B. Li, G. Yadava, J. Hsieh, "Quantification of head and body CTDIVOL of dual-energy x-ray CTwith fast-kVp switching," Medical Physics **38**, 2595-2601 (2011).

[90] Y. Liu, J. Ma, Y. Fan, Z. Liang, "Adaptive-weighted total variation minimization for sparse data toward low-dose x-ray computed tomography image reconstruction," Physics in Medicine and Biology **57**, 7923 (2012).

[91] J. Tang, B.E. Nett, G.H. Chen, "Performance comparison between total variation (TV)-based compressed sensing and statistical iterative reconstruction algorithms," Physics in Medicine and Biology **54**, 5781-5804 (2009).

[92] D.J. Brenner , E.J. Hall "Computed Tomography — An Increasing Source of Radiation Exposure," New England Journal of Medicine **357**, 2277-2284 (2007).

[93] B. Lu, H. Lu, J. Palta, "A comprehensive study on decreasing the kilovoltage cone-beam CT dose by reducing the projection number," Journal of Applied Clinical Medical Physics **11**, 3274 (2010).

[94] L. Zhu, J. StarLack, "A practical reconstruction algorithm for CT noise variance maps using FBP reconstruction," Proc. SPIE **6510**, 651023-651023-651028 (2007).

[95] E.J. Soares, C.L. Byrne, S.J. Glick, "Noise characterization of block-iterative reconstruction algorithms: I. Theory," IEEE Transactions on Medical Imaging **19**, 261-270 (2000).

[96] W. Wang, G. Gindi, "Noise analysis of MAP-EM algorithms for emission tomography," Physics in Medicine and Biology **42**, 2215-2232 (1997).

[97] J. Qi, "A unified noise analysis for iterative image estimation," Physics in Medicine and Biology **48**, 3505-3519 (2003).

[98] J.A. Fessler, "Mean and variance of implicitly defined biased estimators (such as penalized maximum likelihood): applications to tomography," IEEE Transactions on Image Processing **5**, 493-506 (1996).

[99] Y. Zhang-O'Connor, J.A. Fessler, "Fast predictions of variance images for fan-beam transmission tomography with quadratic regularization," IEEE Transactions on Medical Imaging **26**, 335-346 (2007).

[100] S. Schmitt, M. Goodsitt, J. Fessler, "Fast variance prediction for iteratively reconstructed CT images with locally quadratic regularization," IEEE Transactions on Medical Imaging **PP**, 1-1 (2016).

[101] X. Jia, Y. Lou, R. Li, W.Y. Song, S.B. Jiang, "GPU-based fast cone beam CT reconstruction from undersampled and noisy projection data via total variation," Medical Physics **37**, 1757-1760 (2010).

[102] C. Miao, H. Yu, "A general-thresholding solution for l_{p} (0< p< 1) regularized CT reconstruction," IEEE Transactions on Image Processing **24**, 5455-5468 (2015).

[103] D.S. Lalush, B.M. Tsui, "A fast and stable maximum a posteriori conjugate gradient reconstruction algorithm," Medical Physics **22**, 1273-1284 (1995).

[104] W. Chlewicki, F. Hermansen, S.B. Hansen, "Noise reduction and convergence of Bayesian algorithms with blobs based on the Huber function and median root prior," Physics in Medicine and Biology **49**, 4717-4730 (2004).

[105] C. Bouman, K. Sauer, "A generalized Gaussian image model for edge-preserving MAP estimation," IEEE Transactions on Image Processing **2**, 296-310 (1993).

[106] P. Massoumzadeh, S. Don, C.F. Hildebolt, K.T. Bae, B.R. Whiting, "Validation of CT dose-reduction simulation," Medical Physics **36**, 174-189 (2009).

[107] H.H. Barrett, K.J. Myers, *Foundations of Image Science*. (Wiley-Interscience, 2004).

[108] P.T. Lauzier, G.H. Chen, "Characterization of statistical prior image constrained compressed sensing. I. Applications to time-resolved contrast-enhanced CT," Medical Physics **39**, 5930-5948 (2012).

[109] "ICRU Report No. 87: Radiation dose and image-quality assessment in computed tomography," Journal of the ICRU **12**, 1-149 (2012).

[110] J.T. Dobbins, E. Samei, N.T. Ranger, Y. Chen, "Intercomparison of methods for image quality characterization. II. Noise power spectruma)," Medical Physics **33**, 1466-1475 (2006).

[111] A.A. Sanchez, "Estimation of noise properties for TV-regularized image reconstruction in computed tomography," Physics in Medicine and Biology **60**, 7007-7033 (2015).

[112] S. Rose, M.S. Andersen, E.Y. Sidky, X. Pan, "Noise properties of CT images reconstructed by use of constrained total-variation, data-discrepancy minimization," Medical Physics **42**, 2690-2698 (2015).

[113] P. Thériault Lauzier, J. Tang, G.-H. Chen, "Quantitative evaluation method of noise texture for iteratively reconstructed x-ray CT images," Proc. SPIE **7961**, 796135-796135-796136 (2011).

[114] E.C. Ehman, L. Yu, A. Manduca, A.K. Hara, M.M. Shiung, D. Jondal, D.S. Lake, R.G. Paden, D.J. Blezek, M.R. Bruesewitz, C.H. McCollough, D.M. Hough, J.G. Fletcher, "Methods for clinical evaluation of noise reduction techniques in abdominopelvic CT," RadioGraphics **34**, 849-862 (2014).

[115] C.C. Brunner, S.F. Abboud, C. Hoeschen, I.S. Kyprianou, "Signal detection and location-dependent noise in cone-beam computed tomography using the spatial definition of the Hotelling SNR," Medical Physics **39**, 3214-3228 (2012).

[116] X. Duan, J. Wang, S. Leng, B. Schmidt, T. Allmendinger, K. Grant, T. Flohr, C.H. McCollough, "Electronic noise in CT detectors: Impact on image noise and artifacts," American Journal of Roentgenology **201**, W626-632 (2013).